Thermally Induced Dynamics and Solar Radiation Torque on Deployable Solar Panels of Nanosatellite

THERMALLY INDUCED DYNAMICS AND SOLAR RADIATION TORQUE ON DEPLOYABLE SOLAR PANELS OF NANOSATELLITE

By

Syahrim Azhan bin Ibrahim

Supervisor: **Professor Eiki Yamaguchi**

Department of Civil and Architectural Engineering

A dissertation submitted to Kyushu Institute of Technology in partial fulfilment of the requirements for the degree of Doctor of Philosophy

Graduate School of Engineering

Department of Engineering

Kyushu Institute of Technology

2020

Abstract

Small satellites in low-Earth orbit (LEO) often experience energy constrictions owing to small solar panel areas and eclipse transitions. Much like larger satellites, these small satellites, including nanosatellite class such as CubeSats always opt for deployable solar panels to generate more power. By using deployable solar panels, the satellite's surface that faces the Sun will be more exposed; yet, the force generated by the pressure of solar radiation can disrupt spacecraft orbits. For the time being, the study on deployable solar panels for CubeSats has largely focused on panel configuration, deployment mechanism, deployment mechanics and dynamics, and power harnessing capacity. Meanwhile, when dealing with solar radiation pressure, the interest is largely on its use as a thrust force to control satellite trajectories. An apparent research gap is addressed on the thermal effects of solar radiation, as well as on the increase in solar radiation pressure, to CubeSats with deployable solar panels.

This study is divided into two parts. First, a methodology is presented to predict the types of thermally induced dynamics (TID) that can occur on deployable solar panels of a CubeSat in LEO. A computational method combining finite difference method and finite element method is developed to examine the TID effect on the CubeSat body. A 3U CubeSat with four short-edged deployable solar panels, has been considered. Time historic temperature readings of the solar panels operating in-orbit are obtained using a thermal analysis software. The results are used in a numerical analysis software to identify the structural response of the solar panel. Next, the effect of solar panels' sudden motion on the satellite's pointing direction is examined through a static analysis with inertia relief. A thermal snap motion could occur during eclipse transitions due to rapid temperature changes in the solar panels' cross-sections. In the case of asymmetric solar panel configuration, noticeable displacements in the pointing direction can be observed during the eclipse transitions. This work only examines an LEO mission, where the solar cells on the solar panels are directly exposed to sunlight throughout daylight and pointed to the Earth while orbiting in shadow. Simplification is made to the CubeSat's structure and in some parameters of the space environment. The conducted TID analysis reveals the effect of TID phenomenon on deployable solar panels and the CubeSat's pointing direction. Therefore, in a situation of partial

solar panel deployment, or in an asymmetric deployable solar panel design configuration, the attitude control system designer could anticipate the order of the required magnitude motions to mitigate the disturbance. In addition, the methodology developed in this research can be applied to simplify the study of TID on satellite appendages.

In the second part of the study, solar radiation torque characteristics consequential from the solar panels' enlarged surface on the CubeSats are investigated. Three commonly used, commercially available solar panel configurations are introduced and their reference missions are established for comparative purposes. The software algorithms used to simulate various orbital situations are described in detail and some issues are highlighted based on the observed results. The solar power generated for each corresponding configuration is also presented. The obtained data on solar radiation torque and generated solar power are intended to be used by designers of nanosatellite to predict the characteristics of solar radiation torques to be encountered and the solar power to be generated when applying a variety of deployable solar panels; hence, aiding them to choose appropriate panel configuration and attitude control system for their design. Furthermore, the methodology and algorithm employed should provide insight on how to develop the source code for calculating the in-orbit solar radiation and solar power.

Acknowledgment

My thanks and appreciation to my advisor, Prof. Eiki Yamaguchi. Throughout this work his guidance and advice were invaluable. His generous attention and continuous support are greatly appreciated.

My appreciation is also due to the committee members for their inputs on the research, Prof. Mengu Cho, Prof. Kazutoshi Matsuda, and Prof. Hideo Nagase. I would like also to thank Prof. Kusuo Kato for his help in experimental work. My deep appreciation also goes to the members of Structural Lab of year 2015-2019 for their assistance in my study, support, and friendship throughout my stay in Japan. I am especially indebted to Mr. Hiruaki Nishio for all his generous help in getting my family settled down in Japan. Similarly, thank you to the wonderful admin staff at Engineering Office.

This work was sponsored by Public Service of Malaysia to whom my thanks are due. Special appreciation to National Space Agency Malaysia which introduced me to the fascinating world of satellite technology and space engineering.

Lastly, my thanks and appreciation to my family. To my parents, for their whole support and love, they have given. I never have made it here without both of them. To my wife, Liana, for her constant patience and understanding. And to my three daughters, Sarah, Sofia, and Suraya for their companionship in Japan.

Table of Contents

List of Figures

List of Tables

List of Abbreviations

aF	Albedo Factor
CG	Cover Glass
CTE	Coefficient of Thermal Expansion
ECI	Earth-Centred Inertial
HST	Hubble Space Telescope
ISS	International Space Station
JAXA	Japan Aerospace Exploration Agency
JD	Julian Date
KOMPSAT	Korea Multi-Purpose Satellite
LVLH	Local Vertical Local Horizontal
NASA	National Aeronautics and Space Administration
RAAN	Right Ascension of the Ascending Node
SC	Solar Cells
SINDA	Systems Improved Numerical Differencing Analyzer
SP#	Solar Panel
TID	Thermally Induced Dynamics
TD	Thermal Desktop

Chapter 1: Introduction

The usage of solar cells to generate electrical energy from the sun is a primary source of power for most operational satellites within the Solar System. Normally, implementing a satellite mission requires compliance with the limits imposed by energy production. Progress has been made in the form of more efficient solar cells and deployable solar arrays that can increase the surface area exposed to the sunlight. The former has been available for some time, but the latter is only common for large satellites, such as communication satellites and many other commercial satellites. For small satellites, early missions have been focusing on education and science endeavors, which normally can be catered by solar cells attached to the outer surface of a satellite's body. However, as newer missions have become more complicated, and significantly leaning towards technological missions, the requirement for more power has become necessary. In fact, insufficient power generation has been reported as one of the causes of small satellite mission failures [1]. Therefore, the technology of deployable solar panels, previously only used by large satellites, is now considered essential for small satellites too. Owing to that, an investigation is required to characterize the effects of possible disturbances that are commonly associated with spacecraft equipped with solar arrays.

This research firstly investigates the phenomena of thermally induced dynamics (TID) on deployable solar panels on a nanosatellite segment of a small satellite known as CubeSat, which operates in low Earth orbit (LEO). Next, the increased solar radiation torque because of the enlarged surface area exposed to sunlight is examined. Findings are beneficial to satellite mission designers whose payloads or communications systems have strict pointing requirements.

This chapter starts with section 1.1, with regard to the motivation for the research, followed by section 1.2, covering the literature review, while section 1.3 explains the objectives, scope, and approach. Next, the contribution of the study is described in section 1.4, whereas the succeeding chapters of the thesis are summarized in section 1.5.

1.1 MOTIVATION

Back in 2000, there were only 5 known small satellite projects, but the trend had increased significantly to 80 by the year 2013 [1]. This is mainly due to the shift toward using nanosatellite class known as CubeSat, first introduced in 1999. Nowadays, CubeSats are an established "kit" for small satellites and the concept requires no introduction among the space-exploring community. Over 70% of small satellites launched from 2012 to 2018 were CubeSats i.e. 961 in total, which have dominated the small satellite market [2]. This increase in launches has also led to an increase in the type of mission, such as for a scientific experiment, for a demonstration of advanced technology, and for a precursor mission of a future space project [1,3,4]. Subsequently, enhanced performance in the area of power generation is required, which led to the growing demand of deployable solar panels.

The inclusion of deployable structures on a spacecraft can introduce a number of attitude control problems that would not have existed otherwise. While the experienced dynamics and solar radiation torque have been a subject of study in various literature, the focus had been on large satellites, with size, mass, and power requirements being many levels larger than a typical CubeSat. Given this apparent research gap, the following questions are addressed in this dissertation:

i. *How can the attitude motion of a CubeSat, mounted with deployable solar panels be affected by TID phenomena?*

ii. *How much increment on external disturbances will the CubeSat experienced when using the deployable solar panels?*

This research answers these questions using numerical simulations in two separate studies.

1.2 LITERATURE REVIEW

As mentioned in the motivation section, additional to the increase in power requirement, other complexities arise with the use of deployable solar panels on CubeSats. Complications are mainly due to the constraints on size, dimension, and cost of the CubeSats. In this section, the literature review describes recent research pertaining to deployable solar panels on CubeSats. The literature can be categorized into three groups. The first group focused on deployable solar panel structures and

construction. The second group concentrated on the dynamics related to deployable solar panels, while the third group mainly focused on the main purpose of using such panels i.e. to maximize solar power generation. Based on these previous works, the current study attempts to add more value to this field by focusing on the phenomena of TID, and additional disturbances due to the usage of deployable solar panels. Hence, some other works related to solar radiation forces are also reviewed in this section.

1.2.1 Research on deployable solar panel structure and deployment mechanism

To simplify the attitude-pointing control system, it is preferable to use body-mounted solar cells on a satellite, especially to avoid the complexity of adding a Sun-tracking mechanism. Moreover, it would further reduce complications associated with deploying the mechanism. However, due to the small surface area of the CubeSat, there is limited space to mount solar cells, resulting in a relatively low power generation. According literature, the estimated power that can be obtained from body-mounted solar panels and advanced triple-junction solar cells on a 3U CubeSat is lower than 10W [5]. Therefore, to increase power generation, the use of deployable solar panels coupled with accurate attitude-pointing system is necessary. The recent development in the miniaturization of attitude-control systems [6,7] should be capable of pointing and manoeuvring accurately, to cater to high performance missions that demand power for accomplishment.

Deployable panels are developed for nanosatellites to enhance their power generation capabilities. Commercially available panels have typically been tested and proven to function in orbit. Usually, they come together as part of a CubeSat system and are very convenient, not only for new and inexperienced participants to the CubeSat community, but also for payload-oriented teams who are focussed on the novelty of results. Since there are many CubeSat developers, one developer's panels and power systems are not necessarily compatible to those of others. The panels come with various geometries and mechanisms of use. Some are based on their previous customer's missions, and therefore, could be specific for certain orbital satellite scenarios that meet distinct requirements for stabilizing attitude. The most straightforward system is built on a single-stranded solar panel, connected to the CubeSat body by a single hinge or two (e.g. [8–11]). One of the earliest 3U-sized CubeSat launched to orbit, the Delfi-C^3 nanosatellite, introduced various innovative technologies in its flight experiment.

Among them was the usage of a new space-dedicated Copper Indium Gallium di-Selenide (CIGS) solar cells on a titanium substrate [8]. CIGS is a type of thin film solar cell (TFSC) with higher specific power (W/kg) and lower storage volume (W/m3) compared to ordinary GaAs and Si-based solar cells for space application. In addition, the TFSC is said to have a higher tolerance for the emission of charged particles. Among TFSC-type solar cells, CIGS is claimed to be the most suitable type for space application. In order to hold the CIGS cells, an innovative interconnected scheme based on contact pressure between the cells was produced to diminish stresses among the electrical contacts. Using the contact pressure signified that no external forces can act on the electrical contacts, hence minimizing pressures among the layers. On the other hand, this stress or pressure could occur if welding and soldering methods were used. Similar to this panel design is the one introduced by Pumpkin Space Systems [9], in which their solar panels are assembled to the CubeSat's body using their trademarked CubeSat hinge design. Their solar panels can be deployed at user specified angles (45º to 90º).

In the meantime, Vertat and Vobornik [10] proposed a blossom-like deployable solar panels configuration to complement the wall-mounted solar panels on its 1U PilsenCUBE CubeSat. Small springs and a burnable cable are used to deploy four double-sided coated panels, secured in a closed position during the launch. The solar panels use a highly efficient triple junction GaInP2/GaAs/Ge in the form of small triangle strings, also known as triangular advanced solar cell (TASC) developed by the Spectrolab Company. TASC cells are small in size, which allow for many cells to be assembled on a solar panel. As the number of cells per panel is high, the cells can be interconnected through multiple lines to establish redundant string interconnection. The redundancy is particularly important as a countermeasure against in-orbit power generation failure, solar string failure, or switch regulator failure. These deployable panels can increase power generation up to 7.04W, which is a significant improvement compared to the 2.47W power generation without deployable solar panels. They managed to increase the mean power and minimum power twice as high. Furthermore, it is now feasible to include an active attitude-control system to point the panels toward facing the Sun. The overall design overcame the constraint of the CubeSat's structure and introduced a simple assembling technology to keep the cost low. Another new

design for a deployable solar panel that could enhance electricity generation for a nanosatellite was propositioned for application in another 1U CubeSat; KufaSat [11]. The proposed design consists of four extendable panels, which have two solar cells on each side of every panel i.e. a total of sixteen solar cells. With the new deployment mechanism, it was expected that the new power generation could be increased to 270% at maximum exposed area to sunlight and 294% at minimum exposed area to sunlight compared to the original design without the extendable panels. Additionally, compared to the original design, the charging current to the batteries could be increased to 280% at maximum exposed area to sunlight, and 300% at minimum exposed area to sunlight. Although the new deployment system increased the CubeSat's weight by 35g, the benefit to power generation certainly outweighs this minor setback.

McGuire et al. [12] proposed a deployment system design which creates a plane of solar panels to collect energy using mechanical hinge mechanism for the OpenOrbiter CubeSat. The panels are attached to the top of the CubeSat's main body and open from there. This hinge supports interoperability with the power system of the CubeSat by facilitating electrical power transfer through it. This deployable solar panel design also has a similar design to the side panel design, hence only minor modification is needed to add the hinge to the CubeSat. The hinge is a custom-made spring-loaded modified barrel hinge, which integrates two locking mechanisms. In the first stage, the deployment rotation spring and mechanical stopper secure the panel in its closing position. Secondly, a spring-loaded locking pin automatically positions itself when the hinge is in the fully deployed position. This deployable solar panel system allows for a 235.8% power output over the optimal positioning of the OpenOrbiter's base design. The additional hinge and panels design increased the weight to about 72 grams, which is considered minimal considering the significant improvement in power generation obtained.

Systems with more complex configurations normally consist of a number of interconnected solar panels [5,13–15]. In the Xatcobeo project, a mechanism called panel deployment mechanism (PDM), which consists of two sets panels in one deployable solar, panel is implemented on a 1U CubeSat [13]. The first panel (PDM1) deploys first and the second panel (PDM2) unfolds after the PDM1 is successfully opened. The design's one new advance is the implementation of a flat spring to halt the initial deployment. The spring prevents micro vibrations caused by movements

that could occur in orbit. The spring has another purpose, to act as an additional blocking system that makes the panel intact. Senatore et al. [14] developed an extendable solar array system called XSAS for a CubeSat package. XSAS is able to supply constant electricity of 23 W on average. XSAS is a novel design due to the integration process of every mechanism, each function within the small CubeSat form-factor, and the integral passive control advantage of the deployed geometry. When undeployed, the solar array is installed compactly within the CubeSat's 1U size, whereas the power bus can fit into a 0.5U volume. The array can passively extend in an "accordion style" to enlarge surface zone. 16 packed solar panels are supported by the current design and payloads of up to 1.5U can be accommodated, all of which fit the maximum size of the 3U CubeSat. Passaretti and Hayes [15] implemented solar array drive assembly (SADA) technology in the design of an articulated solar array drive to address the requirement for maximal energy transmission from a specified solar array assembly. Their mechanism is capable of supporting autonomous sun-tracking which can be realized by using both solar cells and an additional shadow-casting intra-bank barrier. This complete system would consume an estimated 500 mW while conveying the arrays. When inactive, the actuators and system would consume less than 1 mW. Another SADA-based deployable solar panel system was developed for CubeSats by Santoni et al. [5]. The system consists of a segmental hinge and spring mechanism that can be possibly applied in 1U, 2U, 3U, and 6U CubeSats. The deployment engages multiple solar panels linked in a chain and one solar panel is fixed to the satellite's frame structure by a single hinge. However, the deployed solar array has yet to have manoeuvring capability added to track the Sun. Nonetheless, the solar panel's alignment of the body-fixed deployable solar arrays can be arranged variously to boost average power, inclusive of eclipse times.

Currently, steerable solar arrays for CubeSats are already available in the market. Among them are the HAWK solar arrays produced by MMA Design LLC [16] and the Sunmill Array produced by Tethers Unlimited [17]. The former is a single-axis orientable solar arrays, whereas the latter is a multi-degree of freedom spatial mechanism solar array. Another interesting design is the self-orienting solar array for 3U-sized CubeSat proposed by McGill E. [18]. McGill's design is similar to that of Sunmill Array's, in which the deployed solar panels will be lifted up and away from the CubeSat's body by a linkage mechanism, to allow the panels to rotate freely to

some limitation angle without interference. The best part of McGill's design is that this limitation angle can be actuated in a passive manner, with no internal computerization used to control the position of the solar array. This is enabled by the use of a shape memory alloy material called nitinol that is a part of the linkage mechanism (i.e. spring parts) used to link the CubeSat's body and the solar panels. The idea is that the nitinol springs will change shape depending on how much solar radiation they receive, so that the solar panels will be directed to the Sun accordingly. This type of growth that incorporates processes typically used on larger, more complex, and more expensive spacecraft will certainly give more flexibility for various institutions to use smaller and lower cost satellites for more missions.

1.2.2 Research on solar panel deployment dynamics

Studies on the dynamics of solar panels are also a focus of aerospace researchers. Rawashdeh et al. [19] described the design, modelling, and investigation of an attitude control mechanism for a ram-facing nanosatellite in LEO. A 3U CubeSat is intended to preserve one 10x10 cm2 face oriented to the velocity vector during orbit. The solution, which implemented deployable drag fins that bear a resemblance to a space dart design, was revealed to be proficient in supplying passive stabilization for orbits below 500 km. The method to model the rarefied atmosphere and its interaction with the spacecraft body for a range of fin geometries is called a simplified Direct Simulation Monte Carlo. For a 3U CubeSat design with deployable side panels, it is discovered that the best angle for deployment is approximately 50°. For altitudes below 450 km and worst-case orientation inaccuracies of 2.5 degrees at 400 km, stability was maintained. Similar study on orientation control for low altitude triple CubeSat space darts was made by Armstrong et al. [20]. In the study they described a simple orientation control design that utilizes the aerodynamics related to the space dart geometry of a 3U CubeSat with deployable solar panels in a low altitude orbit (< 500 km) to stabilize pitch and yaw passively. The functional altitude reaches a limit when de-stabilizing gravity gradient torque surpasses the aerodynamic torque stabilization, usually occurring at altitudes more than 500 km, dependant on the angles of solar panel deployment and the concentration of surrounding air.

Meanwhile, for the Xatcobeo project, they performed kinematic and dynamic simulations utilising MSC/Adams programme to determine dimension and estimates for the springs incorporated in their CubeSat flight model [13]. As mentioned in the

previous section, the CubeSat consists of two sets of deployable solar panels; PDM1 and PDM2. Therefore, to halt the opening rotation physically, two mechanical restraints are used. The first one is secured to the shear plate to ensure the precise maximum angle for deployment (90º), whereas the stopper is a steel flat spring which secures the panel in the final position to reduce vibration issues. In another research, Peters [21] investigated the dynamics associated with solar panel deployments by providing detailed models and analyses of the forces and motions imparted on a CubeSat body by the deployment of solar panel assemblies. NEi Nastran was used to create and analyse finite element models of individual solar panels. Then, MSC SimXpert was used to generate multi-body dynamics simulation and subsequently to examine the outcomes of deploying solar panel on CubeSat attitude dynamics. Nominal and partial/asymmetric deployments were recreated for four various solar panel assemblies and results were attained for the evolution of the angular velocities and accelerations of the CubeSat for the duration of the deployment.

Bettiol [22] investigated dynamic analysis of thin film solar panels on small satellites. According to her study, the primary downside of thin solar panels is the tremendous flexibility that signifies very low first natural frequencies for the panels. Such frequencies can, in some instances, match with orbital frequencies, or can be provoked by regular manoeuvres that can cause significant instability, compromising power generation and spacecraft attitude. Her study considers the consequences of the primary orbital disturbances on the orientation of a small spacecraft with two large flexible attachments. The panels are separated into a number of rigid bodies, linked to each other by rotating joints, while the spacecraft is considered as a solitary rigid body. The collected findings reveal the needed torques for the satellite to maintain a specific attitude and the torques diffused from the panels to the central structure. Her study also includes a dispersed control action supplied by smart active films lateral to the length of the panel. According to the results of the performed simulations, a control system on the panels brings benefits to the behaviour of the central structure. Piezoelectric patches or wires, as well as other electroactive materials bonded to the panel, could provide an effective control on the system, damping unwanted vibrations and reducing the displacements of the panels tips. Their lightness and low power requirements offer the possibility of maintaining the advantages of thin modules, such as low mass, low stowage volume, and high-power density. Nevertheless, the mass reduction of a

controlled system is more significant in a small satellite. On the contrary, on a large satellite the mass penalty due to the increasing thickness of a stiffened panel becomes irrelevant.

Blandino et al. [23] created a vertical software application using multibody dynamics software to improve model creation and reduce the run time of simulations. To achieve this goal two objectives were met. The first is to design an overall automation procedure that can proficiently focus on the comprehensive hinge assembly model and replicate its range of movements, while obtaining data on stiffness for all angles of freedom and to translate the data to outline a straightforward but precise nonlinear point-to-point force to be used in the solar array assembly model. The second objective is to develop and simulate a high-fidelity system-level prototype of the deployment sensitivities in a deployable solar array that was designed to be used with a 6U CubeSat. The deployed CubeSat solar array model also undergoes simulated tests to determine the maximum tumbling rates that can be tolerated before the deployed solar array configuration becomes unstable. The simplification of a hinge with complex geometry to a single nonlinear component allows a nonlinear finite element representation to be used for each of the solar panel, while maintaining a reasonable simulation time.

1.2.3 Research on solar panel power production

The power subsystem and the communication subsystem are the most critical parts, which can cause malfunctioning in many cases [10]. It is due to high power requirements during the data transmission and a low reliability power supply, which is not able to cover it. Many CubeSat groups work only with simplified calculations of accessible solar power. These calculations consider the maximum and minimum nanosatellite cross-section value of solar cells, count the mean value of cross-section, and count the mean power through nominal solar cells efficiency. For more accurate calculations of a nanosatellite's accessible power, it is necessary to identify some important solar cells behaviours, which are unpublished. For example, efficiency dependence on the cells' temperature and efficiency dependence on the sunlight incidence angle are not to be neglected. Continuing from the new deployable solar design previously proposed for PilsenCube [10], Vertat et al. [24] proceeded with a more detailed study on dependencies and on improved calculations of the accessible solar power in the TASC cells that they used. In the paper, they described five different

calculations of the available solar power from the TASC solar cells in a configuration, which is typical for CubeSat nanosatellites. According to them, it is not possible to neglect some solar cell efficiency dependencies for a simplification of calculations, as it could lead to an overestimation of the available solar power onboard the nanosatellite and to the potential orbit failure due to low energy supply. Maximum difference between a simplified calculation and their improved calculations reaches 25%. Such a high level of power overestimation could be critical in the nanosatellite's design. So, for a correct prediction of the available solar power on board the nanosatellite, it is necessary to measure the unpublished temperature and angle efficiency dependencies.

Horvath et al. [25] described the physical layout of solar cell arrays intended to maximize power production in orbit, together with the thermal classification procedures applied throughout the thermal optimization of the body. The objective is to design a solar array body for particular orbital assignments with maximal thermal conductance while retaining the array's small size. The former is particularly important because it would optimize the power generation of the solar array. The most typically adapted material is FR4 due to its mass-effectiveness, with a density of 1850kg/m^3, but with a very low thermal conductivity at 0.8 W/mK. Aluminium has been suggested for usage, possessing a very high thermal conductivity at 237.7 W/mK. Despite Aluminium's higher density than that of FR4 (Aluminium alloy 7075T6 density = 2810 kg/m^3), it has been utilised widely in space technology. The procedure led to an improved solar array design, which was effectively applied in the Masat-1 CubeSat mission, reinforced by flight telemetry data concerning the temperature values of solar cell. The solar cells' surface temperature and their thermal gradient are substantially decreased, ensuring a very low possibility of solar cell delamination. From simulations, solar power generation can be boosted by 10% in comparison with other FR4-based solutions.

Self-shadowing can occur from various viewing degrees and would reduce energy generation in space-dart-configured CubeSats. This parameter is influenced by the angle of the panels and their orientation toward sunlight. The latter is also a function of the attitude and the orbit parameters. Lee D.Y. et al. [4] created an innovative energy generation design, and developed a system of simulation that assesses a variety of roles with the objective to describe power handling for intricate nanosatellite models. Specifically, in the study, a 3U space dart CubeSat with four

deployable panels, was taken as an example design problem for optimization. The design employs a spacecraft-frame-fixed spherical coordinate procedure to review the intricate geometry of a satellite's self-induced shadowing with calculation supplied by the Open Graphics Library. The solution is capable for a comprehensive search of the solar panels' angle of deployment that can maximize power generation. From there, the developed simulation system can also determine ways to maximize total energy, to maximize the minimum average power per orbit, and to minimize the discrepancy in power generation. Their results show that orbit geometries and the photovoltaic panel angle specifications can cause varying power output on a space dart design beyond 40%. For example, in a sun-synchronous, dawn–dusk orbit at 700 km, they projected a top average power output of 13.86W, whereas, for a non-synchronous orbit, the projected top average power output was 9.6 W.

Meanwhile, Sanchez-Sanjuan S et al. [26] described the kinematic and dynamic calculations to acquire the CubeSat's orientation, together with the mathematical model derivation of solar cells and batteries to compute the power being generated and stored. The incident solar energy was projected by defining the attitude of a 3U CubeSat without deployable solar panels over an orbit; hence, the produced power from the solar cells and the extra power collected in batteries using a direct energy-transfer design. The estimated power consumption was also included, which anticipated all of the satellite's functioning manners and diverse orbital constraints. These approximations were made for three orientation setups: nadir-pointing, Sun-pointing, and free-orientation. The estimated incident average solar energy for the three scenarios specified that the Sun-pointing and free-orientation setups produce more power than the nadir-pointing scenario. This inference will assist in the prediction of the batteries' charging capability during standby mode, for a better confirmation of the required time for the batteries to be fully-charged, prior to the functional modes of the CubeSat.

1.2.4 Other Studies on Solar Radiation

The force generated by the pressure of solar radiation can affect spacecraft orbits. In this section, some of the literature on small satellites, which use solar radiation pressure for thrust in order to meet their missions are reviewed. The first one is the satellite formation flight that applies solar radiation pressure. At present, there is great fascination in allowing multiple small satellites to fly in cluster, trailing, or

constellation formations to work together to achieve the goal of a bigger, generally more costly satellite. Bandyopadhyay et al. [27] have reviewed future small satellite missions with regard to flying formation extensively. Noticeably, most of the small satellites either have no propulsion at all, or use gas propulsion systems to maintain positions. Williams and Wang [28] made an exception by proposing a fresh non-propulsive method for opposing the variant orbital plane precession, a primary formation perturbation caused by oblateness. Oblateness of the Earth, is one of the long-term perturbation effects that must be rectified for a formation to persevere. The applied method employs the solar radiation pressure to act on a rather small exterior, named solar wing, that is secured to a small satellite. The consequential torque can cause a precession of the orbit, and if the solar wing has an average correct size, the perturbation will cancel with that due to oblateness, so maintaining the formation without use of propellant.

Meanwhile, Mishne and Edlerman [29] discussed the viability of utilising drag and solar radiation pressure for a collision-avoidance manoeuvre. For a propulsion-less satellite in LEO, orbit manoeuvring depends on drag and solar radiation pressure. The satellite can perform manoeuvres by orientating it in a way that the forces of both drag and solar radiation pressure will combine to take full advantage of the modification in the semi major axis from a non-manoeuvre case. Subsequently, the orbital period will change and the satellite will avoid the collision ultimately after enough revolutions. The control algorithm requires adequate data on the cross-sectional surfaces of the satellite from all directions, along with the properties of drag and solar radiation. To deal with these natural forces, there must be a difference between the maximum (S_{max}) and the minimum (S_{min}) value of the cross-sectional area. Numerical computation done to a 6U sized CubeSat, in the altitude ranging from 600 to 800 km show that the method is feasible. In less than three days of manoeuvring, the accumulated along-track aberration is enough to decrease the possibility of collision to a satisfactory level.

Last but not least, solar sailing, which employs solar radiation pressure for thrust, is arguably the most attention-grabbing study in this area. Solar sail propulsion utilizes the solar radiation pressure applied by the momentum transfer of reflected photons to create a net force on a spacecraft. The idea to utilize the radiation pressure for solar sailing to planets in the inner solar system or to near-earth asteroids can be traced back

to the mid-20th century [30]. However, only as recent as 2010, IKAROS i.e. the pioneer interplanetary solar sail spacecraft was successfully demonstrated by the Japan Aerospace Exploration Agency (JAXA) [31]. IKAROS' mission is to showcase solar sail propulsion in interplanetary space, and is considered as a breakthrough in solar sail advancement [32]. Solar sail missions on the CubeSat standard have also been proposed and developed [33–36], although the primary objective is to demonstrate the sail deployment technology as well as to de-orbit to Earth's atmosphere. This is due to restriction on the size of the CubeSats, hence the sail is much smaller in size than the IKAROS' sail. In August 2019, The Planetary Society announced a successful mission of the LightSail 2, after the CubeSat successfully deployed its solar sail and ascend to its orbit with the power of sunlight [37]. Despite the fact that the technology is still in early development, the key benefit of solar sails is the potential cost reduction in transportation. Therefore, supplementary comprehension and quantification of cost reduction for using solar sails are extents of attention for forthcoming research [32].

1.3 OBJECTIVES, SCOPE, AND APPROACH

As mentioned in the motivation section, the study is separated into two parts as described below:

1.3.1 Thermally induced dynamics study

This study aims to predict the types of TID phenomena that can occur on deployable solar panels of a small form factor satellite, CubeSat, placed in LEO. A computational method combining finite difference method and finite element method is developed to examine the TID effect on the CubeSat body. A 3U CubeSat with four short-edge deployable solar panels is considered. Time historic temperature of the solar panels throughout the orbit is obtained using a thermal analysis software. The results are used in a numerical analysis software to ascertain the structural response of the solar panel. Next, the effect of solar panels' sudden motion on the satellite's pointing direction is examined through a static analysis with inertia relief. This work only examines a LEO mission where the solar cells of the solar panels point to the Sun throughout the daylight period and point to the Earth while in shadow. Simplification is made to the CubeSat's structure and some parameters in the space environment.

1.3.2 Solar radiation torque study

This study examines solar radiation torque characteristics consequential from the solar panels' increased area on the CubeSats. Three commonly used, commercially available solar panel configurations are introduced and their reference missions are ascertained for comparison. The software algorithms employed to simulate various orbit situations are described in detail and several issues are emphasised on the basis of observable outcomes. Additionally, the solar power generated for each corresponding configuration is also presented.

1.4 RESEARCH CONTRIBUTIONS

The main contributions of this dissertation are the development of a systemic approach for the checking of the disturbances on CubeSats. In the TID study, a computational method is developed, which fully uses thermal analysis software to characterize temperature field on the orbiting deployable solar panels of a CubeSat and to analyse the type of TID phenomena that can be experienced. The method used is also capable of determining the distortion level on the pointing direction of the satellite. Therefore, in a situation of partial solar panel deployment, or in an asymmetric deployable solar panel design configuration, the attitude control system designer could anticipate the order of the required magnitude motions to mitigate the disturbance. In addition, the methodology developed in this research can be applied to simplify the study of TID on satellite appendages.

Meanwhile, in the solar radiation torque study, a software algorithm is developed and applied to estimate torque disturbance and solar power production. The obtained data on solar radiation torque and generated solar power are intended to be used by designers of nanosatellite to predict the characteristics of solar radiation torques to be encountered and the solar power to be generated when applying a variety of deployable solar panels; hence, aiding them to choose appropriate deployable solar panel configuration and attitude control system for their corresponding mission assignment. Furthermore, the methodology and algorithm employed should provide insight on how to develop the source code for calculating the in-orbit solar radiation and solar power.

1.5 THESIS OUTLINE

The remaining sections of this dissertation are outlined as follows. Chapter 2 presents the TID discipline and a developed simulation system that fully uses thermal

analysis software. Chapter 3 begins with reviews on the need for solar radiation torque study on a small form factor satellite. A software algorithm is then developed in order to assist CubeSat designers and creators in selecting appropriate deployable solar panel configurations for their CubeSats and to anticipate probable disruption forms that could disturb the satellite's mobility. Finally, the dissertation is summarized, and insights for future work are provided in Chapter 4.

Chapter 2: Thermally Induced Dynamics of Deployable Solar Panels of Nanosatellite

2.1 INTRODUCTION

Evolution of small class satellites like CubeSats from educational tools to a platform for technology demonstration and scientific instrumentation has envisioned the idea of using it for more advanced missions such as earth observation and space telescope [1,3]. Such missions require high power, hence the deployable solar panels have begun to be used to accommodate them. However, some earlier larger satellites with deployable solar arrays which occupy the LEO had experienced disturbances that interfered with their missions. One of the major disturbances is thermally induced dynamics (TID) which occurs as a result of changes in solar array panels' cross-sectional temperature differences in the space environment [38].

As shown in Figure 2-1, a satellite which travels around the Earth will experience periodic heating and cooling in the sunlight and shadow regions of the Earth with variations of the thermal environment. The front and rear sides of the solar panels receive a different amount of solar radiation which gives rise to cross-sectional temperature differences in the solar panels. This will result in a differential thermal

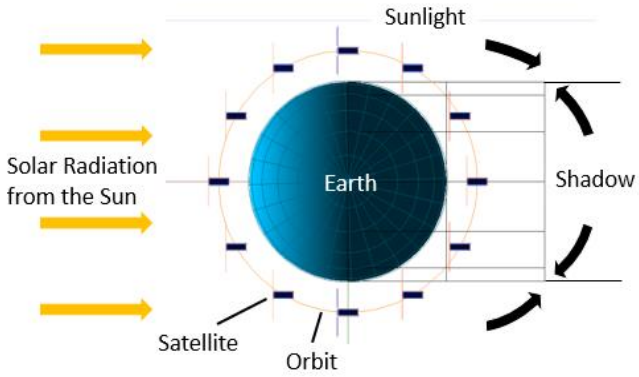

Figure 2-1. The in-orbit thermal environment of a satellite

expansion that can cause thermo-elastic deformations. Slowly developing temperature differences lead to quasi-static deformation whereas sudden heating changes can induce temperature gradients that generate an impulsive torque resulting in a dynamic

response [38]. Subsequently, these motions could result in rigid body rotation of the entire satellite due to the conservation of the total angular momentum of the system.

One of the earliest satellites recorded having TID problem was OGO-IV spacecraft in the 1960s [38]. Since then, there were many research works done on establishing analytical and numerical methods to investigate the problem especially after the event of a pointing jitter induced by thermally driven bending of the solar arrays on Hubble Space Telescope (HST). Thornton's group systematically examined the TID on HST in the 1990s. Firstly, they developed an analytical approach to determine the thermal-structural response of a flexible rolled-up solar array due to sudden increase in external heating [39]. The analyses consist of an uncoupled thermal-structural analysis that assumes the heating and temperature gradients are not affected by thermally induced motions and a coupled thermal-structural analysis that includes the effects of structural deformations on heating and temperature gradient. During the period, the TID has been classified into four categories, namely, thermal bending or quasi-static deformation, thermal snap, thermally induced vibrations and thermal flutter [38]. In the case of a deployable solar panel, quasi-static deformation is a bending motion that occurs because of slowly varying temperature differences in its cross-section. As the temperature differences develop slowly, the bending acceleration is very small and therefore, inertia force is negligible. Hence, they should not affect satellite attitude dynamics. This deformation can easily be recognized by out of a plane distortion of the panel's faces. The other three motions normally occur when solar panels are subjected to a rapid rise and decay of cross-sectional temperature differences due to rapid changes in thermal loading such as when a satellite exits from or enters into the Earth's shadow. In a thermal snap, the dynamic response results in only non-vibratory large transient deformation whereas for the thermally induced vibration, dynamic response results in a stable vibratory motion following the initial large transient deformation. Thermal flutter is an unstable thermally induced vibration response caused by coupling between incident heating and structural deformations. It is most severe, as the deformation could generate vibrations of increasing amplitudes, which can cause the satellite to experience unexpected large motions. Because of that, attention on the stability criterion of the dynamic response for the satellite appendages is important. Parameters for this criterion consist of the ratio of thermal and structural response times, the solar inclination angle and the system damping [39,40]. In addition,

Duan et al. [41] formulated that the thermal structural analysis considering both the radiation and geometric nonlinearity of satellite appendage could also cause the thermal flutter phenomenon.

Next, the investigation was extended into the effects of TID disturbance on the attitude dynamics of a simple spacecraft consisting of a rigid body with a cantilevered flexible appendage [42]. The formulation is based on a generalized form of Lagrange's equations for hybrid coordinate dynamical systems. Numerical results show pointing error and superimposed oscillations developed to the attitude response of the system due to TID. Later, laboratory investigation was made on the thermal snap disturbances experienced by the Upper Atmosphere Research Satellite solar panels [43]. The solar panel size article is about one-third of the actual size. Using finite element analysis, the results showed the correct forecast of the thermal snap phenomenon observed in the solar panel experiments. Other notable successful experiments include the work by Iwata et al. [44] for Advanced Land Observing Satellite solar array and Lee et al. [45] for HST's solar array by using smaller scaled models in their investigations. The comparison of the analytical solution, finite element analysis, and experiment result revealed that the short-term transient of the temperature difference during eclipse transition was important for simulating the TID of the solar array.

In recent time, models used in the TID analysis have evolved from just simplified beams and panels into composite solar arrays which incorporate interaction among components subjected to space heat flux. Shin et al. [46] conducted transient analyses to predict the thermal distortion of the Korea Multi-Purpose Satellite (KOMPSAT) solar array including degradation effects of composite materials during its orbital motion. They found out solar arrays with graphite-epoxy composite face sheets are beneficial with regards to weight savings, temperature distribution, and thermal distortion when compared to those with aluminium face sheets. Meanwhile, Li and Yan [47] detailed differences in TID characteristics of a solar array using graphite epoxy components and stainless steel components. Depending on the satellite mission, the study could provide guidance for designers to optimize the structure used in minimizing the influence of space thermal environment. Other advancements include the work by Liu and Pan [48] who take into account the effect of satellite rotational motion into the previous coupled thermal-structural analysis. In addition to quasi-static deformation, thermal snap, and thermally induced vibration, this model can also show

the thermally induced fluttering effect. Other than that, Azadi et al. [49] studied the vibration suppression of a smart flexible satellite moving in a circular orbit by attaching piezoelectric layers to solar panels as actuators using simulations. By applying a control voltage to the actuators, the panel vibrations can be damped and the amplitudes of these vibrations converge to zero.

All this available research focused on large satellites whose size, mass and power requirements are in orders of magnitude larger than miniaturized size satellites like CubeSats. There is an apparent lack of studies on how this phenomenon could affect the CubeSat attitude motion although the usage of deployable solar panels has become more popular in recent time [1,3]. So far, available literature on deployable solar panels of nanosatellite only consist of the deployable solar panel configurations [5,50], the dynamics associated with solar panel deployment [21] or the optimization of power generation [4]. Given that most of the CubeSats launched with deployable solar panels have symmetric configurations, there is an assumption that any motion induced by the same disturbance load should cancel each other [21]. Their deployable solar panels' size is much smaller compared to model parameters in previous studies made, which means the effect might be small too. Nonetheless, the aforementioned experiments on the scale model show that the problem could still be induced [43–45]. Furthermore, in anticipation of future advanced mission requirements, prior investigation regarding TID is worthwhile so that necessary countermeasures can be implemented if required.

This study aims to investigate the types of TID phenomenon that could occur on deployable solar panels of a CubeSat and to predict its effect on the pointing direction of the satellite body. The remaining part of this chapter is organized as follows. The analysis model will first be described. After that, the thermal environments in LEO for the orbiting solar panel according to its flight attitude are defined and the resulting time historic temperature is presented. This result is then applied in numerical simulation to predict its impact on the solar panel. Then, the impact of TID on the CubeSat pointing direction is analysed using inertia relief method.

2.2 ANALYSIS MODEL

CubeSats are a class of satellite called nanosatellites, mostly designed for research and technology demonstration purposes [1,3]. They are built to standard dimensions of 10 cm cube for one unit (1U) size with no protuberant parts at launch

[51]. A 3U CubeSat is basically composed of three 1U CubeSats stacked lengthwise. The CubeSat design used in this study is a 3U CubeSat with four identical short edge deployable solar panels as depicted in Figure 2-2. In the figure, Solar Panel (SP) SP1 is symmetric to SP3 while SP2 is symmetric to SP4. Its satellite body has a mass of 3kg. Each panel has a span of 300×100 mm in size area. It has a solar cell assembly consists of cover glass (CG), solar cell (SC) and adhesive, mounted on a composite material FR4 as shown in Figure 2-3. Each deployable solar panel is deployed and fixed by a hinge at a 90º angle with respect to the main structure.

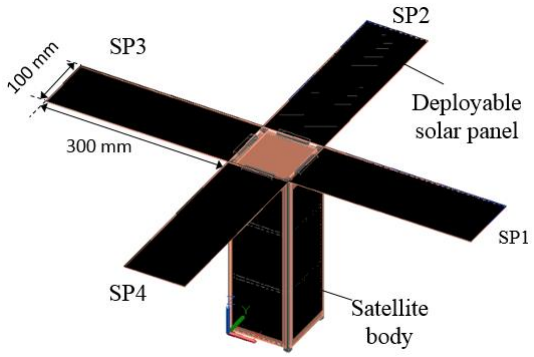

Figure 2-2. Model of 3U CubeSat with deployable solar panels

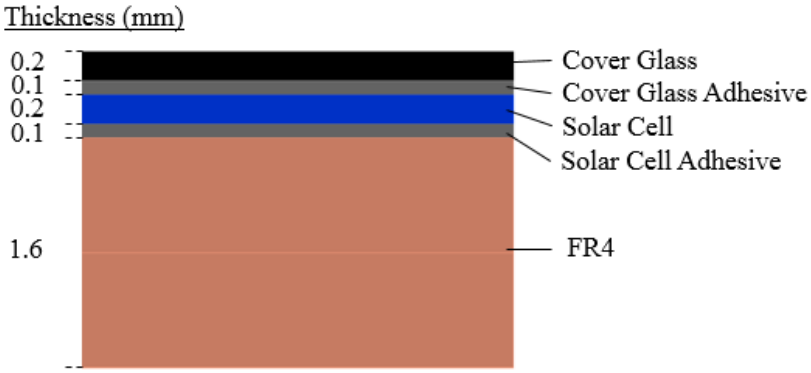

Figure 2-3. Sectional view of the solar panel

The thermal properties and mechanical properties of the solar panel used in this study are listed in Tables 2-1 and 2-2, respectively. For thermal analysis, typical material properties considered are density, thermal conductivity, and specific heat. These properties are used to determine the rate of temperature change in the solar panel when combined with their environment. Meanwhile, thermo-optical properties dictate how the solar array emits, absorbs, transmits and conducts thermal energy. For structural response analysis, other than density, additional properties required are

Young's modulus, shear modulus, Poisson's ratio and coefficient of thermal expansion (CTE). The FR4 material is assigned orthotropic properties while the other materials have isotropic properties. Orthotropic material orientations for FR4 are defined by the subscripts 1, 2 and 3 that correspond to x, y and z coordinates system, respectively. Information is gathered from various literature and datasheets [46,52–56]. For a solar cell, not all incident solar energy at its surface will dissipate into heat. A portion of them is converted into electricity and the parameter is known as solar cell efficiency. Therefore, the absorptivity value of the solar cell in Table 2-1 is actually the effective absorptivity value that has taken into account the solar cell efficiency.

Table 2-1. Thermal properties of different materials for the solar panel

Material	Density (kg/m^3)	Thermal Conductivity (W/m K)	Specific Heat (J/kg K)	Absorptivity	Emissivity
Cover glass	2600	1.4	737	0.95	0.88
Cover glass adhesive	1100	0.15	1030	-	-
Solar cell	5315	48	360	0.696	0.85
Solar cell adhesive	1100	0.15	1030	-	-
FR4	1900	0.29	1200	0.64	0.82

Table 2-2. Mechanical properties of different materials for the solar panel

Material	Young's Modulus (GPa)	Shear Modulus (GPa)	Poisson's ratio	CTE (1E-6)
Cover glass	75	30.74	0.22	7
Cover glass adhesive	6	2.31	0.3	54
Solar cell	84.8	32.37	0.31	5.7
Solar cell adhesive	6	2.31	0.3	54
FR4	$E_1 = 25.4$ $E_2 = 21$ $E_3 = 21$	$G_{12} = 11$ $G_{13} = 0.7$ $G_{23} = 11$	$\nu_{12} = 0.162$ $\nu_{13} = 0.138$ $\nu_{23} = 0.138$	$\alpha_{11}= 20$ $\alpha_{22}= 20$ $\alpha_{33}= 86.5$

Properties mismatch between the materials composing the solar panel, characterized by different stiffness and CTEs will cause thermo-elastic deformations when exposed to day and night temperature differences [57]. Under simulated space environments, composite material degradation used on the solar array of the KOMPSAT had been documented by Shin et al. [46]. Due to the decrease in strength, stiffness and CTE values of the composite material, they simulated using a finite element software that out-of-plane deflections along the central line of the solar arrays

model are reduced after 80 thermal cycles in simulated LEO environmental system. On the other hand, on-orbit degradation of the solar array of a Japanese satellite named Suzaku was reported as the cause of the increase in solar cell temperature, thus reducing the current output [58]. The problem occurred after more than five years of operation. In theory, the increase in the temperature could cause a higher expansion of the solar array. However, the properties used in this study are assumed not degraded by exposure to the space environment due to short-lived nanosatellite operational lifetimes average [1]. Nowadays, space qualified commercial off-the-shelf solar panels with radiation tolerance longer than average lifetimes of CubeSats, as well as space heritage record [59–61], can be obtained to ease CubeSats developers concern on reliability matter.

2.3 THERMAL ENVIRONMENTS ON SOLAR PANELS

An orbiting satellite can be heated externally by space environment and internally from the satellite body itself. At LEO, the Sun and Earth are the primary environmental sources. These heat sources are classified as solar flux, Earth-reflected radiation (albedo) and Earth-emitted radiation [38]. Ideally, during daylight, the solar cell side should face the solar flux directly to receive as much solar energy as possible. In the meantime, the Earth-albedo and Earth-emitted radiation are radiated to the backside of the solar panels. The in-orbit heating condition during daylight is depicted in Figure 2-4. Meanwhile, the solar panels cool themselves by emitting heat radiation to

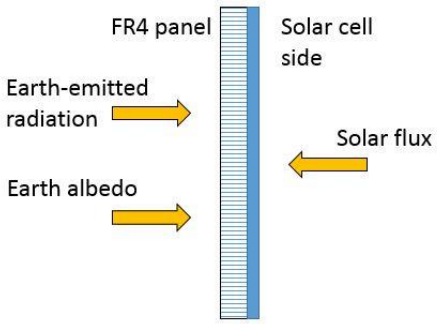

Figure 2-4. External heating conditions on a solar panel during daylight

deep space. For this study, the solar flux in Earth orbit and the Earth-emitted radiation are kept constant at 1,354 W/m^2 and 221.5 W/m^2 respectively for simplification. The Earth-albedo depends on the solar albedo factor (aF), which is defined as the fraction

of solar radiation reflected by Earth. The aF value varies both seasonally and geographically, but it is fixed at 0.35 in this work.

The orbital profile of the CubeSat for this study in an LEO orbit with details defined in Table 2-3. Approximately, it takes about 92 minutes to make one complete revolution around the Earth. Specifically, the CubeSat flies in sunlight and in shadow for about 57 and 35 minutes, respectively in one orbit period. Temperature variations at the CubeSat surfaces could fluctuate at a range of –150 to 150 ºC. Such changes in temperature could lead to both severe sudden heating and sudden cooling not less than 30 times a day.

Table 2-3. Orbit data

Orbit Altitude	400 km
Orbit Inclination	56°
Right Ascension of the Ascending Node (RAAN)	335.4162°
Argument of Periapsis	132.0472°
Eccentricity	0.0005054
Orbital Period	5549 s

Normally deployable solar panels of CubeSats have only one degree of freedom angular motion, hence cannot be actively controlled to face the sunlight. Reason being the lack of space to install motorized actuators normally used by large satellites to rotate the panels, as CubeSats have to comply with strict form-factor requirements to fit into a common deployment system called a Poly-PicoSatellite Orbital Deployer [51]. CubeSats must change their orientation to ensure optimal pointing of the solar panels to sunlight, although usually, the pointing requirement of its payload must take precedence. In this work, we consider a mission where the solar cells of the deployable solar panels point to the Sun throughout the daylight period and point to the Earth while in shadow. In such setting, both maximum power generation by the solar panels and maximum sudden heating changes on the solar panels during eclipse transitions are expected. The orbit trajectory is illustrated in Figure 2-5 with respective solar panels assigned to labels as in Figure 2-2.

2.4 THERMAL ANALYSIS AND RESULTS

Temperature profile analysis is performed using an orbital space thermal analysis software Thermal Desktop (TD) [62], Systems Improved Numerical

Differencing Analyzer (SINDA) [63]. In TD, finite difference and finite element objects are combined with environment definitions in AutoCAD's three-dimensional design environment. TD creates the node and conduction networks, launches SINDA for the solution, and provides post processing results. The thermal mathematical model of the satellite is the same as in Figure 2-2.

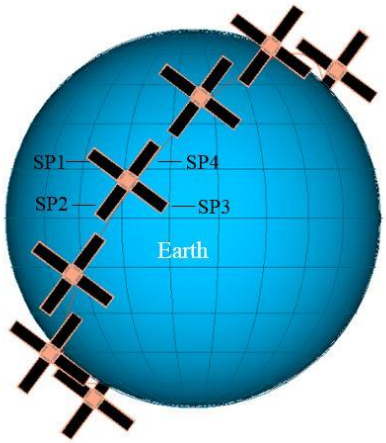

Figure 2-5. Orbital profile of the CubeSat from the Sun view

In this study, the objective of the thermal analysis is to obtain the temperature average on different layers of the deployable solar panel as a function of orbit time. Each deployable solar panel is attached to the satellite body as an appendage. For ease of analysis, conductive heat transfer from the satellite body is neglected. Temperature average rather than temperature field would be sufficient, as differences are expected to be minor due to the small surface size compared to the external heat radiation received. Therefore, each layer except the FR4 layer is set as a single lumped mass node. The FR4 panel is divided into two nodes; namely, top and bottom nodes to discern temperature differences between both the front and back surfaces of the panel. In total, each solar panel is represented by six nodes. Other than that, the initial temperature of the whole solar panel is set at 237 K. Contact conductance is included in the model and is set to 1 W/K from one layer to another layer. The temperature of the hinge that fixes the solar panel to the satellite body is always set at 303 K whereas the outer space temperature is set at 4 K. Transient solution option is chosen in SINDA calculation. By default, SINDA will perform a transient thermal analysis by implicit forward-backward differencing, where one heat balance equation is written about a diffusion node as a forward finite difference equation and another as a backward finite difference equation. The resulting sum of these two equations is:

$$\frac{2C_i}{\Delta t}(T_i^{n+1} - T_i^n) = 2Q_i + \sum_{j=1}^{N}\left[G_{ji}\left(T_j^n - T_i^n\right) + \hat{G}_{ji}\left(\left(T_j^n\right)^4 - (T_i^n)^4\right)\right]$$

$$+ \sum_{j=1}^{N}\left[G_{ji}\left(T_j^{n+1} - T_i^{n+1}\right) + \hat{G}_{ji}\left(\left(T_j^{n+1}\right)^4 - (T_i^{n+1})^4\right)\right] \qquad (2.1)$$

where T_j^n is the temperature of node *j* at the current time *t*, T_j^{n+1} is the temperature of node *i* at the next time $t + \Delta t$, G_{ji} is a linear conductor attaching node *j* to node *i*, $\hat{G}_{ji}$ is a radiation conductor attaching node *j* to node *i*, C_i is the thermal capacitance of node *i*, and Q_i is the power input source to node *i*. Effectively, Eq. (2.1) uses the average of the temperature derivatives at the current and next times to predict the overall temperature change.

We first discuss the results of thermal analysis of one panel, i.e. SP1. Figure 2-6 shows the total external heat flux absorbed by the top (CG) and bottom (FR4 bottom) surfaces, which is the sum of solar radiation, Earth-emitted radiation, and Earth-albedo. During the shadow period, the incident heat flux on the top surface is derived from the Earth-emitted radiation. When the CubeSat flies toward the Sun, alternately the bottom surface is heated by this radiation, as well as the Earth albedo. Meanwhile, the top surface is immediately heated by solar flux as it is in the normal direction with sunlight.

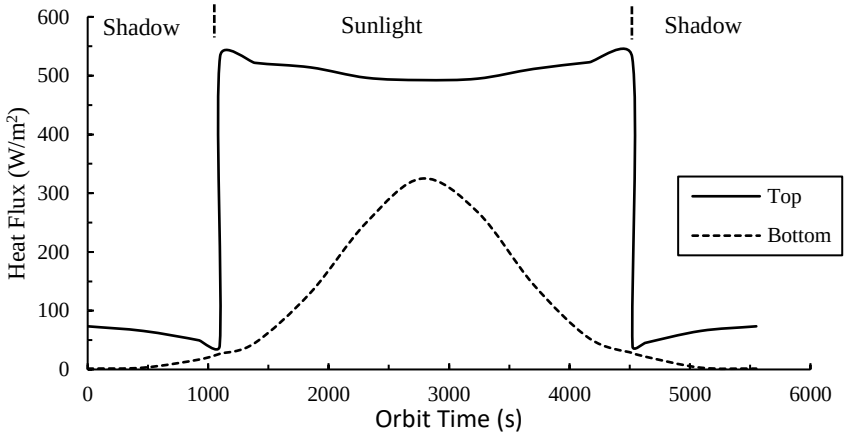

Figure 2-6**.** Absorbed heat flux on the top and bottom surfaces of the deployable solar panel in one orbit period

Results of temperature profiles taken at the 1-second interval on SP1 are shown in Figure 2-7. The measurement begins when the CubeSat is positioned halfway across the Earth's shadow region and lasted for two orbit period. It can be observed that due

to the change of heat flux absorbed along the trajectory, the temperature of the solar panel varies accordingly. In the shadow region, the temperature of the solar panel is greatly reduced by the absence of solar flux radiation and Earth-albedo. As a result, the entire solar panel structure is almost at the same temperature. However, changes occur when they enter the sunlight region as their temperature will increase differently depending on the position of layers and material properties. The temperature variation with orbit time on the surface of the CG are ranging from 215.0 to 352.3 K. The solar cell registers 215.0 to 343.5 K. For the FR4 panel, its top surface registers temperature variation ranging from 215.1 to 333.4 K while the bottom surface registers temperature ranging from 214.7 to 331.9 K.

Meanwhile, temperature differences between the CG layer and the back surface of the FR4 panel are shown in Figure 2-8(a). Sudden temperature differences can be seen

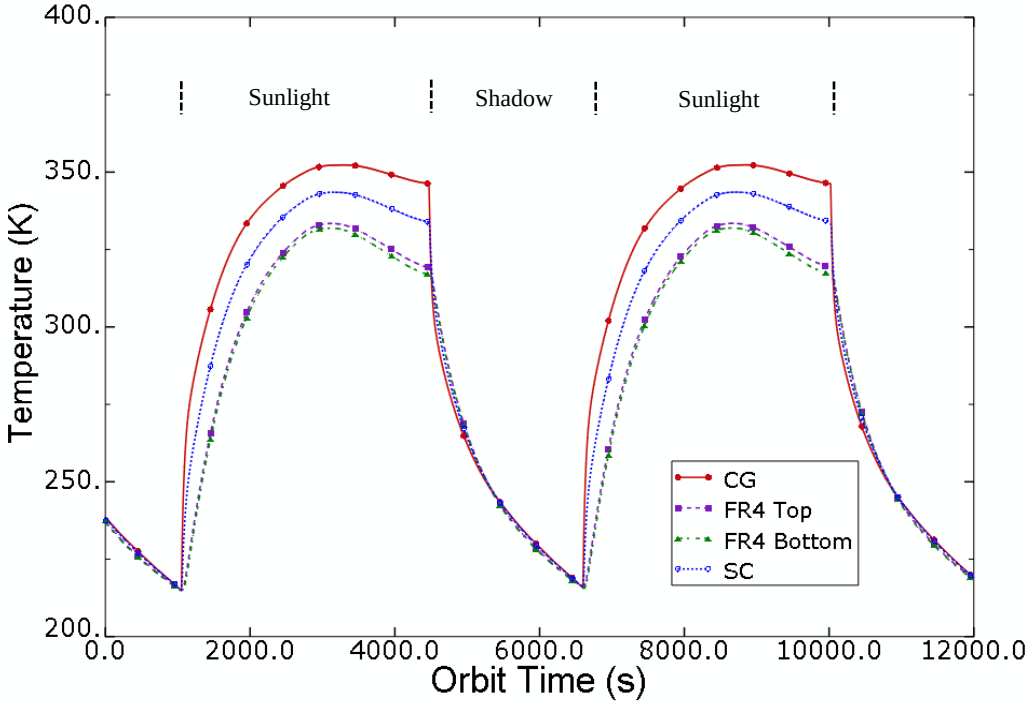

Figure 2-7. Temperature profile of the solar panel (SP1) in two orbit periods

clearly during the transition period of shadow to sunlight and vice versa. Figure 2-8(b) shows the close-up temperature difference during the transition from shadow to sunlight region during the orbit time from 1,020 s to 1,220 s. The temperature difference exhibits an exponential response that is typical of a first-order system subject to a step input. The steady state temperature difference is about 50 K. The rapid

change of temperature gradient could induce thermally induced vibration on the solar panel. The critical parameter which reflects temperature change rate is called thermal time constant, $t_{thermal}$ which is the time at which the temperature reaches 63.2 percent of the span between the initial value (0 K) and the steady-state value [64]. From Figure 2-8(b), the $t_{thermal}$ value is about 28 s. The effect of rapid temperature change on the solar panel will be further examined in the next section.

In addition, as previously informed in Section 2, the current CubeSat has four identical fixed-type deployable solar panels. The top surface temperature of each solar panel can be found in Figure 2-9. According to data obtained from SINDA, due to the in-orbit locations and operation attitudes of the CubeSat, direct solar flux absorbed by SP3 is higher than others, hence the higher temperature. Meanwhile, each bottom side of the solar panels is blocked differently by the satellite bus, therefore, the heat absorbed from Earth albedo and Earth-emitted radiation is varied. Furthermore, reflected radiation by the side solar cells also contribute to the temperature variations. The highest temperature variation between two solar panels registered is approximately 4.2 K.

(a)

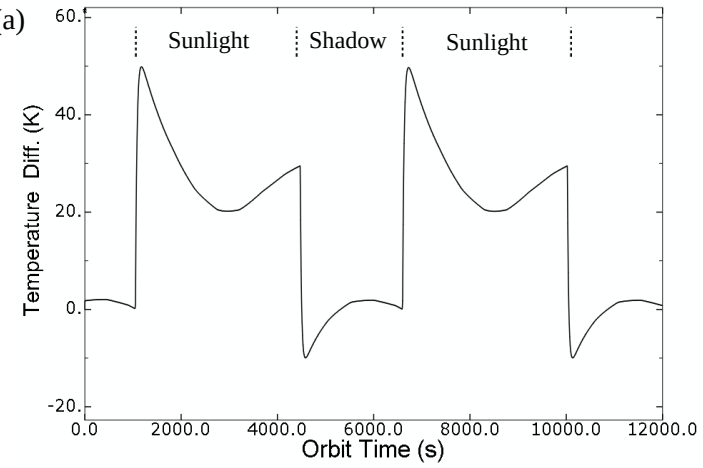

(b)

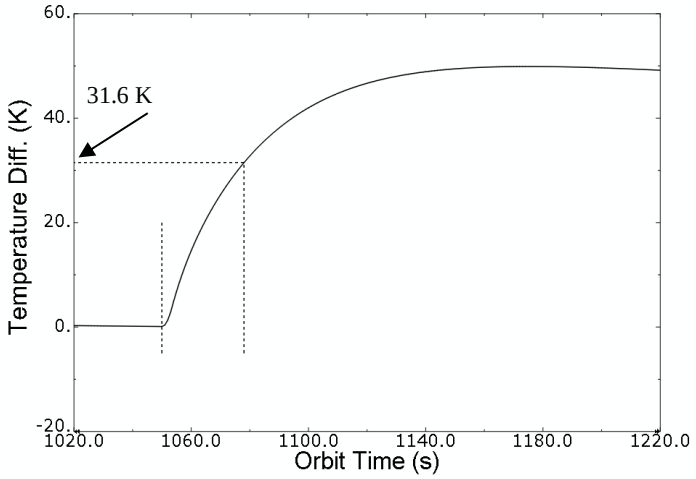

Figure 2-8**.** Temperature differences on the cross-section (a) in two orbit periods and (b) during the shadow to sunlight transition

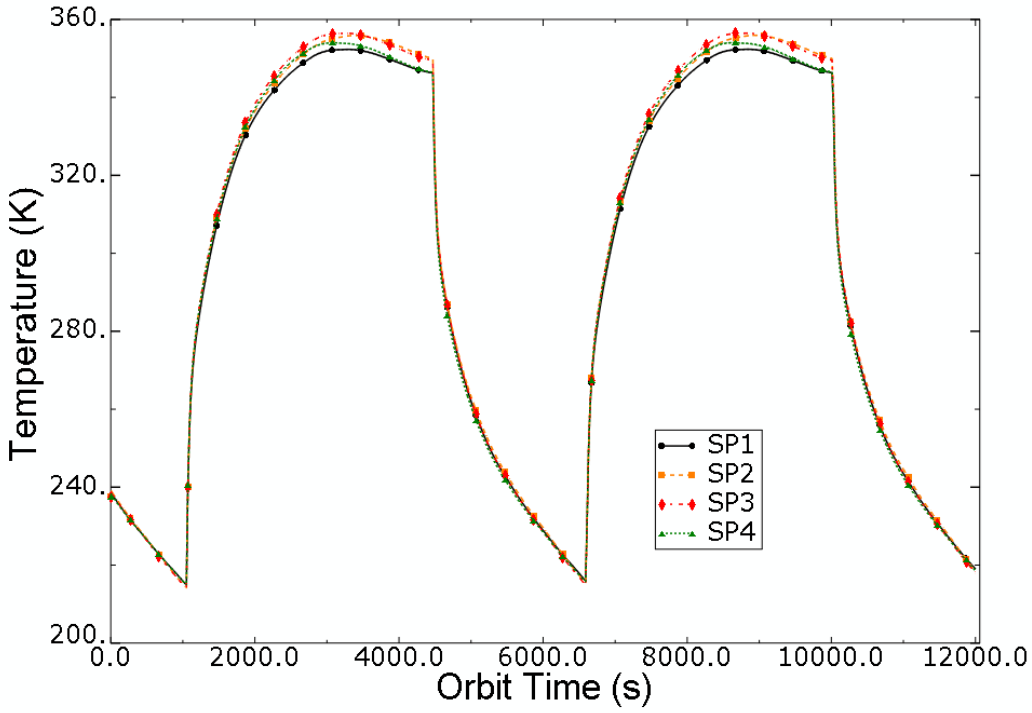

Figure 2- 9. The top surface temperature of all solar panels

2.5 THERMAL STRUCTURAL ANALYSIS OF THE DEPLOYABLE SOLAR PANELS

The objective of the thermal-structural analysis is to classify the types of TID disturbances that may occur on the current CubeSat model and quantify their levels. Even with symmetrical solar panels configuration, non-uniform heating experienced by the solar panels could lead to an unequal level of disturbance, hence producing a non-zero resultant torque among them. Furthermore, the information of thermal disturbance level faced by a solar panel would be useful for example in the case of failed deployment to any of the panels [21]. The SP1 solar panel structural response due to differential heating in its cross-section is investigated and discussed in this section.

A quasi-static response occurs when the solar panel deforms slowly due to the temperature differences across its cross-section at a given instant in time [38]. Based on Euler-Bernoulli assumption that the plane section remains plane under lateral deformation and the transverse shear stress is consequently ignored, for a beam of rectangular cross-section, the quasi-static displacement, v_{qs} depends on temperature difference across its cross-section as follows:

$$v_{qs}(x,t) = -\frac{1}{2}\frac{\alpha_T \Delta T(t) x^2}{h} \tag{2.2}$$

where α is the coefficient of thermal expansion, h is the thickness of the solar panel and, x is the length of the beam and ΔT are temperature differences through the cross-section of the beam. The time historic v_{qs} can be acquired easily if the solar panel is made from a single material. However, as the panel consists of different layers with different material properties (Figure 2-3), a finite element analysis program like the commercially available Abaqus FEA software [65] is used for a more accurate result due to the inclusion of normal strain and shear strain of each direction in the computation [47]. The whole members of the solar panel are modelled using C3D8R element (an 8-node linear brick, reduced integration, hourglass control). The three-dimensional modelling involves expensive computing but is convenient when used to advance this study on three translational degrees of freedom problem to show the CubeSat pointing displacement in Section 6. For mesh controls, hexahedral element and structured technique are chosen. The mesh of the solar panel presented in Figure 2-10 has 10 elements along the width and 30 elements along the length. Three elements through the thickness are used for FR4 layer while the remaining layers used one element each. In total there are 2,100 elements and 4,092 nodes used. Tie constraints on surfaces were applied between layers of the solar cell, as well as to the FR4 panel to couple their motion to each other. One end of the panel has a constraint on all displacements and rotations to simulate a fixed connection to the CubeSat's body. Displacements in the x, y and z axes are set to zero at the centre of this fixed connection.

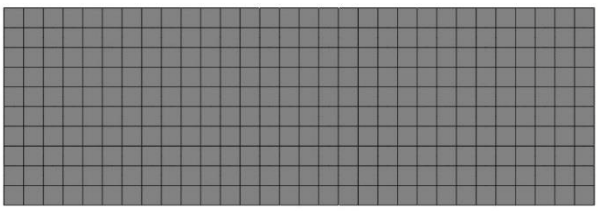

Figure 2-10**.** Finite element mesh of the deployable solar panel

A parameter, B, developed by B. Boyle [64] can be used to determine whether thermally induced vibrations will occur. The parameter is as follow:

$$B = \frac{t_{thermal}}{t_{structural}} \tag{2.3}$$

The structural time constant, $t_{structural}$, is the first vibration period of the structure, found to be 0.0636 s using standard modal analysis in Abaqus. The first three vibration modes

of the solar panel are shown in Figure 2-11 using a standard modal analysis in Abaqus. With $t_{thermal}$ = 28 s, the ratio of thermal response time to structural response time obtained is much greater than 1 s. Therefore, the occurrence of thermally induced vibrations should not be of concern at all and the structural response can be determined

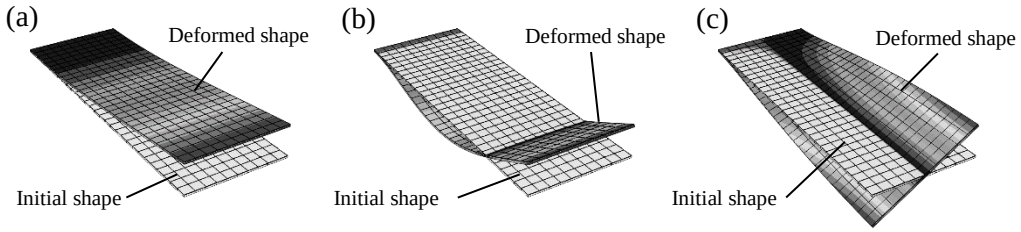

Figure 2-11. First three vibration modes (a) Mode #1 at 15.714 Hz, (b) Mode #2 at 98.264 Hz and (c) Mode #3 at 102.60 Hz

by static analysis. Consequently, the numerical simulation is done using static general analysis in Abaqus rather than dynamic analysis. To satisfy the accuracy demand, the initial integration step is set at 0.0001 s and the maximum integration step is set at 1 s. As in Section 3, the initial temperature 0f 237 K is applied to the whole solar panel. To simulate thermal expansion, predefined temperature variations are applied to each layer of the solar panel using the time historic temperature results previously obtained from TD and SINDA software. For CG, SC and adhesive parts, the temperature difference between the front and back surfaces were found negligible, therefore their respective predefined temperature was set on the whole part. On the other hand, the temperature on the front and back surfaces of the FR4 panel was set differently according to TD and SINDA results. Figure 2-12 illustrates the thermal deformation along the z-axis direction. The displacement due to thermal loading is expected to be the highest at the free end of the FR4 panel, hence two nodes P1 and P2 are set as the points of measurement for all x, y and z-axes displacements.

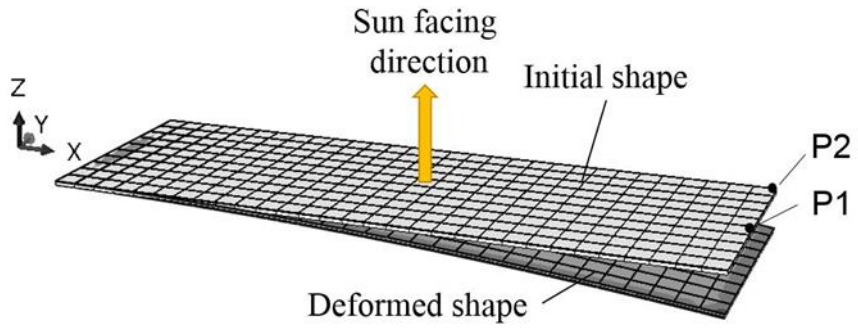

Figure 2-12. Illustration of the thermal deformation

The quasi-static deformation of the SP1 solar panel in two orbit periods are presented in Figure 2-13(a)-(b). Zero values in both figures indicate their respective original positions. In overall, the deformation consists of a succession of equilibrium displacement corresponding to the temperature differences at a given instant time. Figure 2-13(a) shows the quasi-static deformations in x- and y-axes. For both P1 and P2 points, their x-axis displacements are exactly the same and reach maximum level halfway during the sunlight period. Expansion and contraction in y-axis can also be seen by y-axis displacement at P2. Meanwhile, much higher quasi-static deformation level can be seen in the z-axis, as shown in Figure 2-13(b). Most of the time, the panel bends in negative z-axis except at shadow periods. During eclipse transitions, sudden decline and incline in displacement occur in conjunction with the rapid increase and decrease in temperature differences across the cross-section of the solar panel. These conditions will impose a dynamic response from the solar panel. As an example, the dynamic response to the rapid negative displacement using data at point P1 at the time after 1,020 s is further investigated as the highest displacement occurs during the solar panel transitions from shadow to sunlight.

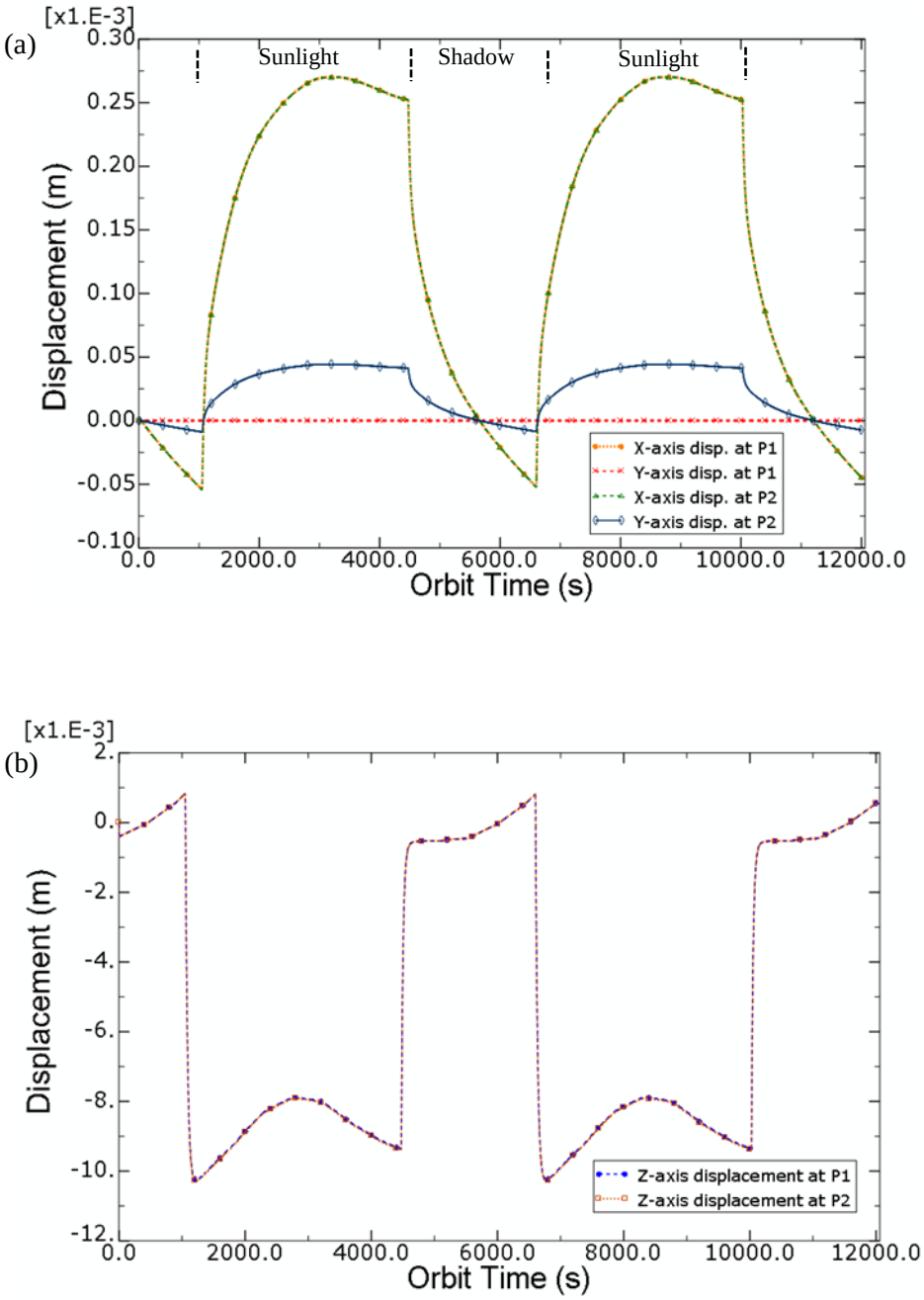

Figure 2-13. Quasi-static deformation of the solar panel at points P1 and P2. (a) The x-axis and y-axis displacements and (b) The z-axis displacements

The solar panel structural response during the shadow to sunlight transition is given in Figures 2-14(a)-(c). Figure 2-14(a) depicts a plot of the point P1 displacement as a function of time. Point P1 displacement reaches a steady state value after about 125 s from its initial position. The solar panel experiences velocity and acceleration transients as the satellite enter the sunlight region. In Figure 2-14(b), the maximum velocity is –3.09 E-4 m/s which occurs at t = 1,055 s. The free end of the solar panel experiences short duration acceleration motions with two peaks at 9.21 E-5 m/s2 and

8.66 E-8 m/s2 but non-vibratory, as shown in Figure 2-14(c). As such, the dynamic response can be characterized as a thermal snap in which the motions are initiated during orbital eclipse transitions and can be observed through its rapid but non-oscillatory appendage deformations.

The numerical results obtained reveal that quasi-static deformation and thermal snap due to rapid temperature change will be experienced by the CubeSat's deployable solar panel along with its orbital motion during eclipse transition. For thermally induced variation disturbance checking, we had actually done dynamic analysis in Abaqus and found that the vibration level has a maximum peak-to-peak amplitude of less than 2.5 E-7 m which is too small to be concerned. In addition to that, the vibration components have stable oscillations which indicate that no occurrence of thermal flutter.

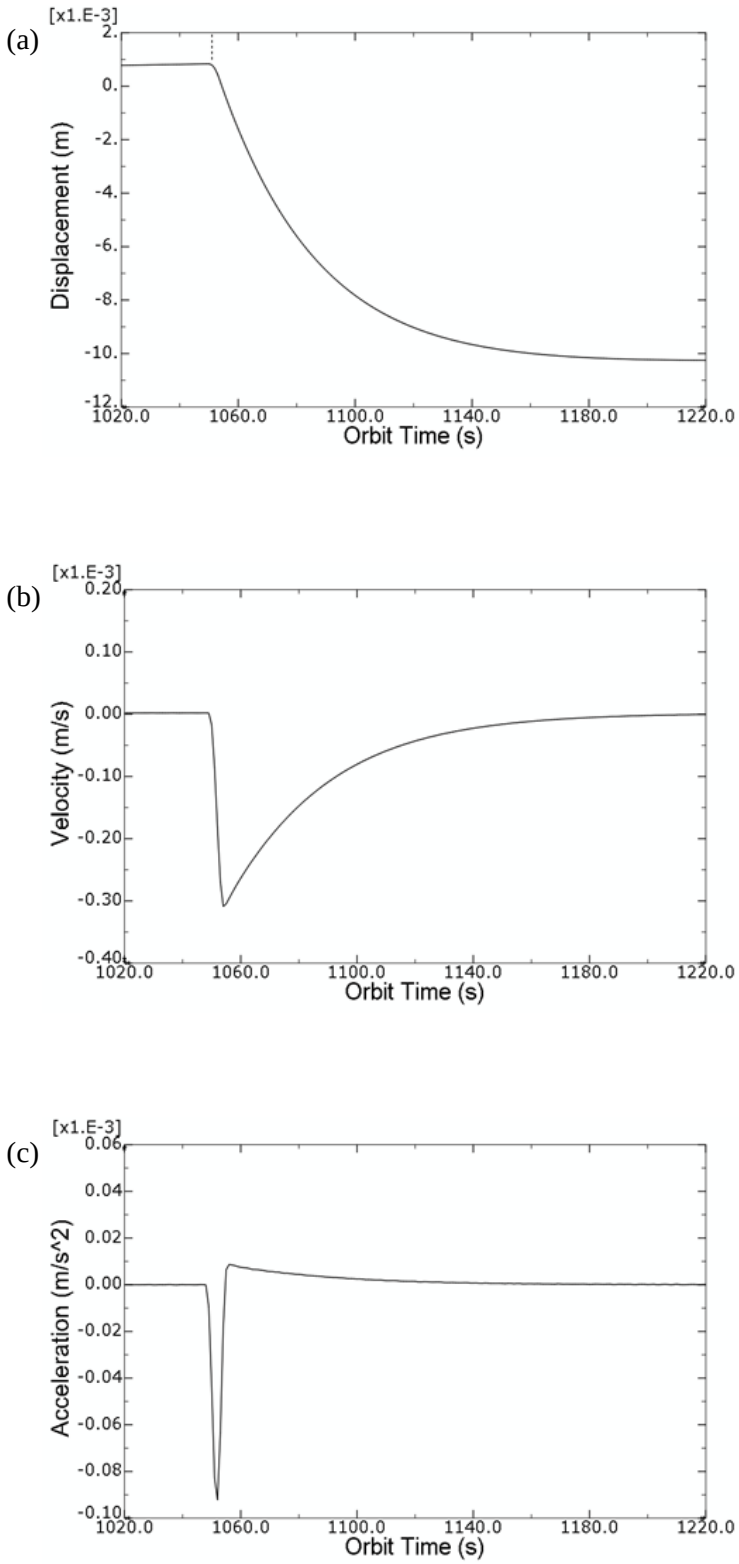

Figure 2-14. Solar panel structural response during shadow to sunlight transition. (a) Solar panel (point P1) displacement, (b) Point P1 velocity, and (c) Point P1 acceleration.

2.6 CUBESAT'S POINTING DISPLACEMENT ANALYSIS

The thermally induced structural motions on the solar panel are known to affect the attitude dynamics of LEO satellites during eclipse transitions [42–44]. The acceleration motion of the solar panel can produce thermally induced vibration torque, which, in turn, will change the orientation of the satellite body in reverse direction to the solar panel motion because of the conservation of angular momentum. In this section, we discuss this effect on the attitude motion of our CubeSat model. Firstly, we consider only one deployable solar panel on the satellite body as shown in Figure 2-15. The satellite body is assumed as a rigid body. A node at the centre of CubeSat's bottom part is taken as the point of displacement check (Point *M*), whereas the centre of mass (C_M) of the satellite is set at the centre of the satellite body. The satellite body has an element size of 0.01.

In this analysis, the inertia relief method is used to find the displacement of point *M* due to a thermal disturbance on the solar panel. Inertia relief is a well-known approach for the analysis of unsupported systems such as air vehicles in flight [66] and satellites in space [67]. Inertia relief involves balancing externally applied forces on a

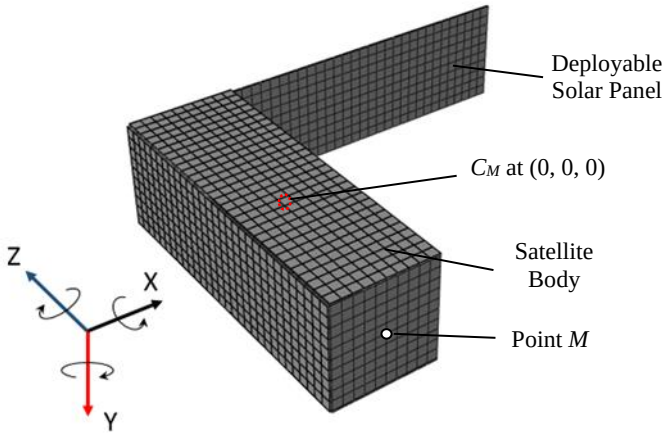

Figure 2-15. 3U CubeSat model with one deployable solar panel for attitude motion numerical simulation

free or partially constrained body with loads derived from constant rigid body acceleration [65]. The basic assumption of inertia relief is that the free-free structure is treated as a rigid body and the acceleration can be calculated by the rigid body dynamics theory. The inertia forces can be recovered and applied at every point of the structure under the dynamic load. Then, the structure is restrained from rigid body motion, and conventional static analysis can be performed. One condition for the

method to give accurate results is that the periods of the dynamic loads are much greater than the periods of the mode of interest in the structure [68]. Furthermore, in Abaqus, it is not necessary for the user to explicitly specify boundary conditions with inertia relief as the boundary conditions necessary to restrain the rigid body modes will be imposed internally at the point in the model that corresponds to the original location of the reference point [65].

In this CubeSat case, implementing inertia relief method should yield exact displacement results as the period of the thermal load is much greater than the periods of the vibration modes of the deployable solar panel structure. For this study, we superimpose the inertia relief load with the thermal load for static analysis in Abaqus. Hence, the inertia relief loading varies with the applied thermal loading. As the solar panel undergoing varying acceleration during thermal loading, the inertia force experienced by the satellite body is included in the static solution through inertia relief loading that balances the external loading. A 200 s temperature historical data of each layer of the solar panel during the shadow to sunlight transition (from 1,020 s to 1,220 s) are set in the predefined field for this analysis. Tie constraint is applied to attach the solar panel to the satellite body. To satisfy the accuracy demand, the initial integration step and the maximum integration step are both set at 1 s. The initial temperature is set at 214 K for the whole CubeSat. Furthermore, no statically determinant boundary conditions are set for the inertia relief analysis. Inertia relief balances externally applied forces on the deployable solar panel with inertial loads developed under steady-state rigid body acceleration. The reference point for the inertia relief method is set at the C_M. As the solid elements, C3D8R do not have rotational degrees, the displacement results at point M are in the form of translations. Rotation can be calculated by simple trigonometry (i.e. Pythagoras's theorem and cosine rule) of the nodal displacement. As depicted in Figure 2-15, the rotations are defined as roll angle for rotation about the x body axis, the pitch angle about the y body axis and the yaw angle about the z body axis.

Figure 2-16 depicts the un-deformed and deformed states of the CubeSat after inertia relief analysis. The deformation scale factor is magnified ten times for a clearer view. The inertia relief procedure is tested on four CubeSat models with 1, 2, 3 and 4 deployable solar panels configurations as presented in Figures 2-17(a)-(d). The first three configurations would be useful in the case of failed deployment to any of the

panels, leaving the CubeSat asymmetric. The difference in temperature of each panel is taken into account in the computation. The results of attitude angle rotations in the form of roll, pitch and yaw angles for each configuration are shown in Figures 2-18(a)-(d).

From the first three results shown in Figure 2-18, when asymmetric configurations occur, slowly developing pointing errors in the direction opposite of the solar panel motion will occur as the satellite body motions are always opposite those of the solar panels. As the temperature difference increased (Figure 2-8(b)), the steady-state value of the pointing error also increased. In Figures 2-18(a) and 2-18(b), rotations occur around the y-axis. Rotations occur around all three axes in Figure 2-18(c). The last result in Figure 2-18(d) shows that even with a complete symmetrical configuration, a slight pitch rotation can still be seen. This is contributed by higher overall temperature in SP3 than SP1. Meanwhile, temperature differences between SP2 and SP4 are too small to cause any obvious effect on the roll angle direction. Results from inertia relief analysis also show that there are upward displacements (in the z-axis) when the CubeSat passes from shadow to sunlight. As shown in Figure 2-19, the more panels deployed in the direction of the Sun, the higher the displacement gets.

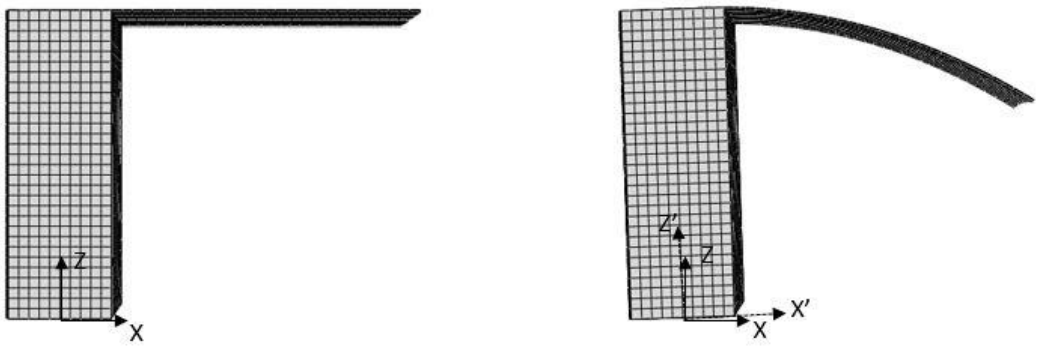

Figure 2-16. Un-deformed and deformed states of the CubeSat

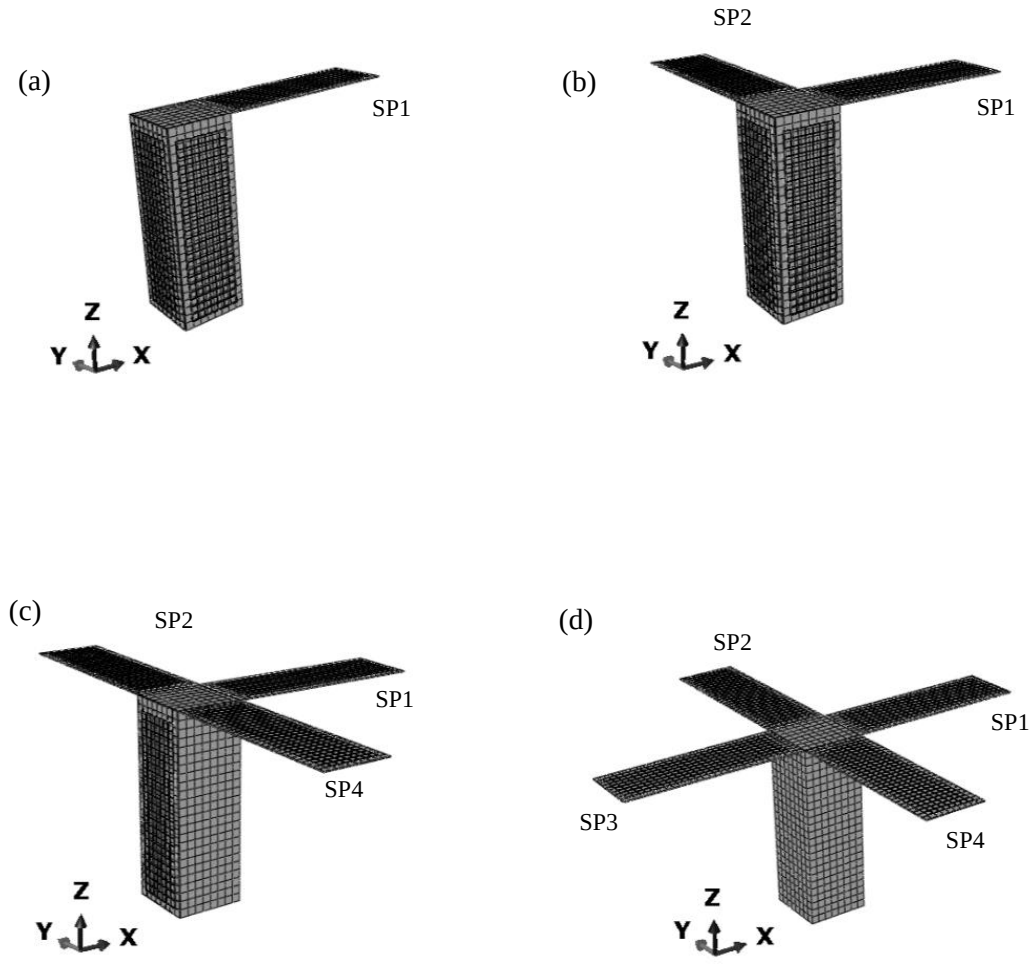

Figure 2-17**.** CubeSat with different deployable solar panels configurations; (a) One deployable solar panel, (b) Two asymmetric deployable solar panels, (c) Three asymmetric deployable solar panels, and (d) Four deployable solar panels.

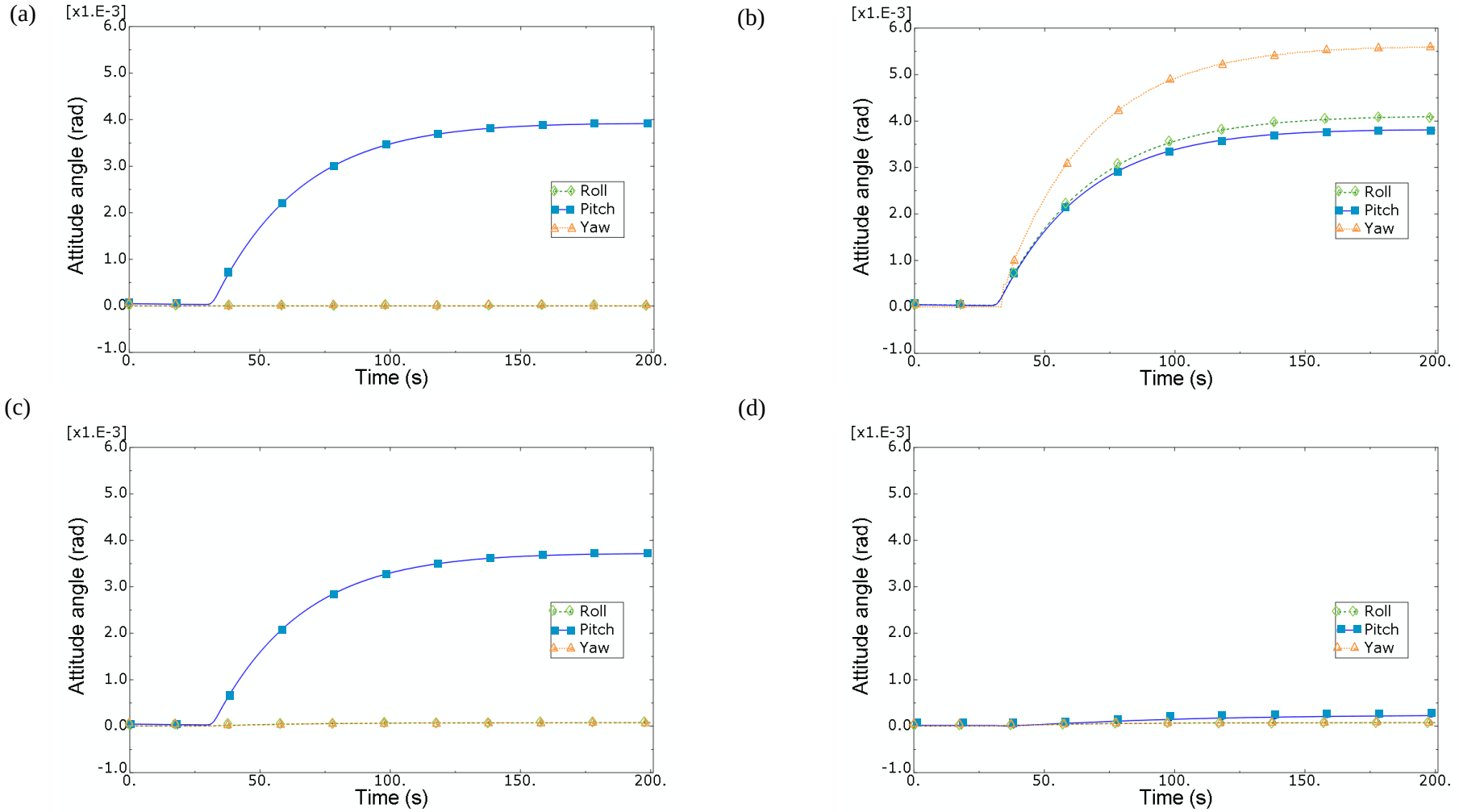

Figure 2-18**.** Attitude angle rotations due to TID on different deployable solar panels configurations: (a) One deployable solar panel, (b) Two asymmetric deployable solar panels, (c) Three asymmetric deployable solar panels, and (d) Four deployable solar panels.

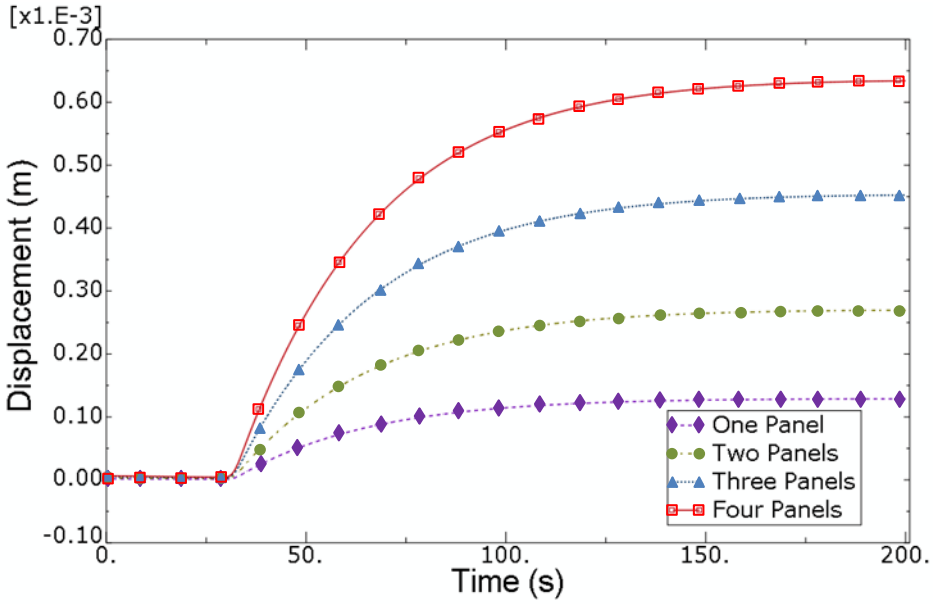

Figure 2-19. Upward displacements of the satellite with different panel configurations during the transition from shadow to sunlight

2.7 CONCLUSION

A computational method that fully uses thermal analysis software to analyse the deployable solar panels of a CubeSat which experienced TID in LEO has been presented. Given the case of the CubeSat model used in this study, simulation results reveal the following facts. First, the solar panels experience quasi-static deformation continuously due to the difference in cross-section temperature. Second, brief thermal snap motions are likely to take place during eclipse transitions. The motion is higher in the shadow to sunlight transition than sunlight to shadow transition. Third, in the case when deployment of the solar panels has failed in getting symmetrical configuration, the satellite will experience pointing displacement during the eclipse transition periods. Finally, symmetrical deployable solar panels design would minimize pointing displacement during eclipse transitions.

Furthermore, the TID analysis done reveals the effect that TID phenomenon can cause to the deployable solar panels and the pointing direction of the CubeSat. Therefore, in the case of partial solar panel deployment failure or with asymmetric deployable solar panel design configuration, the attitude control system designer could expect the order of magnitude motions required to mitigate the disturbance.

Chapter 3: Comparison of Solar Radiation Torque and Power Generation on Deployable Solar Panels Configurations of Nanosatellite

3.1 INTRODUCTION

For satellites in LEO, major sources of external disturbances that perturb their total angular momentum include the gravitational field, magnetic field, atmosphere, and solar radiation. At altitudes of 400 to 1000 km, the disturbances that affect those satellites the most are the gravitational and magnetic torques. Solar radiation can also exert an appreciable disturbance torque in which the level could match the magnitude of atmospheric drag at altitudes over 500 km [69]. The order of disturbance magnitude can significantly increase, especially for satellites with large surface areas. Therefore, the effects of solar radiation should also be a concern for nanosatellites like CubeSats as their missions have become more advanced and subsequently require more power, which has necessitated the use of deployable solar panels. With the addition of these deployable solar panels, the surfaces of the satellite facing the Sun increase and consequently change the characteristics of the total external disturbances on the satellite.

Deployable solar panels on CubeSat can be used to optimize solar power generation and to accomplish specific missions. Many papers about the former application have been published, wherein novel solar panel configurations were designed and solar energy harnessing was studied [4,5,24,50]. For the latter application, in one mission example, the strong atmospheric drag at orbits below 500 km was manipulated to achieve attitude stability [20,70]. The effect of in-orbit temperature variations on the solar cells used by CubeSats has been examined [10], and structure design was proposed to increase the thermal conductance between the solar array and the solid structure of CubeSats to reduce temperature fluctuations [25].

Most of these CubeSats have their own primary missions, and they rely on commercial suppliers for their deployable solar panels as far as reliability is concerned. Whenever deployable parts are involved, products with flight heritage record are

important for increasing the success rate of their primary missions. Although not explicitly specified, some prematurely failed CubeSats missions have been reported, caused by non-functional power subsystems and mechanical deployment systems [1]. We focused on solar radiation torque resulting from the increased area of solar cells on board the CubeSats. In Section 2, solar radiation pressure is briefly explained. In the third section, three deployable solar panel configurations that are commercially available are introduced and their reference missions are established for comparison purpose. Formulations applied to obtain the solar radiation torque-related parameters are described. In Section 4, the computation used in simulation software is described in detail. Subsequently, in Section 5, significant results are presented and discussed. The solar power generation of the different configurations is shown. The work here is useful to help CubeSat developers select suitable deployable solar panel configurations for their CubeSats and to foresee possible disturbance patterns that could affect the satellite motion.

3.2 IN-ORBIT EXTERNAL DISTURBANCES

3.2.1 Solar Radiation Pressure

The solar radiation incident on a spacecraft's surface produces a force that results in a torque about the spacecraft's centre of mass. The major sources of solar radiation pressure are (1) solar flux from the Sun, (2) radiation emitted from the Earth and its atmosphere, and (3) solar radiation reflected by the surface and clouds of the Earth, i.e. Earth's albedo. This radiation (photons) contains momentum that creates pressure on the lit surface of the spacecraft. The solar pressure is:

$$p = \frac{S}{c} \tag{3.1}$$

where *S* is the mean solar flux at 1367 W/m2 and *c* is the speed of light. In the vicinity of Earth, the value of *p* is constant at 4.56 × 10–6 N/m2. Earth-emitted radiation can be assumed as uniform over the surface of the earth. The flux is:

$$q = \frac{400}{\left(\frac{r}{R_E}\right)^2} \tag{3.2}$$

where *r* is the distance between the Earth's centre and the satellite's altitude, and R_E is the earth radius at 6378.165 km. The 400 W/m2 is based on the assumption that the Earth is a black body and has a temperature of 289.8 K. The third source, due to

albedo, is complex because the Earth cannot be treated as a point source as the reflectivity varies over the surface. In this work, the reflection from the earth's surface and from clouds is assumed to be diffuse. The flux due to albedo can then be computed by integrating over the surface of the earth. Therefore, the equation of the flux is:

$$q = \frac{S}{\left(\frac{r}{R_E}\right)^2} aF \tag{3.3}$$

where *aF* is the albedo factor, which 0.33. Of these three sources, solar flux is the dominant source of solar radiation pressure.

To model the solar radiation forces, incident radiation is assumed to be either absorbed, reflected specularly, reflected diffusely, or some combination thereof. In terms of the fractions of the incoming radiation, the following is true for a surface:

$$\rho_a + \rho_d + \rho_s = 1 \tag{3.4}$$

where ρ (optical properties) stands for the fraction of photons that are absorbed, diffusely reflected, and specularly reflected. The force caused by solar radiation can be expressed as:

$$\vec{F} = -pA\hat{s}^T n\left(2\left(\rho_s \hat{s}^T n + \frac{\rho_d}{3}\right)n + (\rho_a + \rho_d)\hat{s}\right) for(\hat{s}^T n) > 0 \tag{3.5}$$

where $\hat{s}$ is the unit sun vector, and *T* denotes its transpose, *n* is the unit normal to the surface, and *A* is surface's area. From Eq. (3.5), the specular component produces the biggest force, followed by the diffuse component and the absorbed component [71]. $\hat{s}^T n$ is the dot product, which is the cosine of the angle between $\hat{s}$ and *n*. Its positive value means that the surface normal faces to the sun direction. Later, we explain that the $\hat{s}$ value is also interchangeable with the other two sources of radiation, which are the Earth's radiation and albedo.

3.2.2 Other Disturbances

To observe how solar radiation torque level changes due to usage of the deployable solar panels, other major disturbance torques in LEO will also be accounted in the study. The disturbances consist of the aerodynamics drag, gravity gradient, and the residual dipole.

Aerodynamic force disturbance is due to the interaction between a planetary atmosphere and a spacecraft surface. The disturbance force model used in this study is:

$$\vec{F} = \frac{1}{2}\rho_{atm} C_D A_p \vec{v}|\vec{v}| \tag{3.6}$$

where ρ_{atm} is the atmospheric density, C_D is the drag coefficient, A_p is the projected area, and $\vec{v}$ is the velocity vector. The projected area for a flat plate is $A_p = A\cos\alpha$ where α is the angle between the surface normal and the velocity vector. The value of ρ_{atm} is $3.725 \times 10^{-12}\text{kg/m}^3$, based on the scale heights atmospheric model [72] whereas the C_D is estimated as 2 [72].

For LEO satellites which have off-diagonal terms in their inertia matrix, they can experience the gravity gradient disturbance torque from the variation of the earth's gravitational force. In the case of nadir pointing satellites, the vector torque is modelled as:

$$\vec{T} = 3\omega_o^2 \begin{bmatrix} -I_{yz} \\ I_{xz} \\ 0 \end{bmatrix} \tag{3.7}$$

where ω_o is the orbital natural frequency. The solar panels would cause off-diagonal terms, but are very small as they are just flat plates.

The residual dipole disturbance torque results from the interaction of the magnetic field generated by current loops on the spacecraft with the Earth's magnetic field. The torque direction, *T*, is normal to both the satellite's residual dipole, *M*, and the Earth magnetic field vector, *B*, as shown in the equation below:

$$\vec{T} = \vec{M} \times \vec{B} \tag{3.8}$$

Both *M* and *B* must be resolved into the body frame [71]. In this study, the magnetic field model is based on a tilted dipole model [72] whereas a 0.01 Am^2 residual dipole strength along the z-axis would be a good estimation from the literature on CubeSats [73]. The total torque disturbances will be the summation of torques due to the solar radiation pressure, aerodynamics drag, gravity gradient, and the residual dipole.

3.3 MODEL PARAMETERS

In this section, the satellite surface parameters that consist of the unit normal to the surface, area of the surface, and the surface optical properties mentioned in Eq. (3.5) are described. Then, the formulations used to determine the unit sun vector are shown. Since an improved solar power generation is always the main purpose for using a deployable solar array, the method to compute solar power generation is also presented so that the results can be compared.

3.3.1 Satellite Configuration

A CubeSat has a standard built dimension of 10 cm^3 for one unit (1U) size with no protuberant parts at launch. A 3U CubeSat is basically composed of three 1U CubeSats stacked lengthwise. For the present analysis, three 3U CubeSat models were configured with deployable solar panels as depicted in Figure 3-1. The models use a

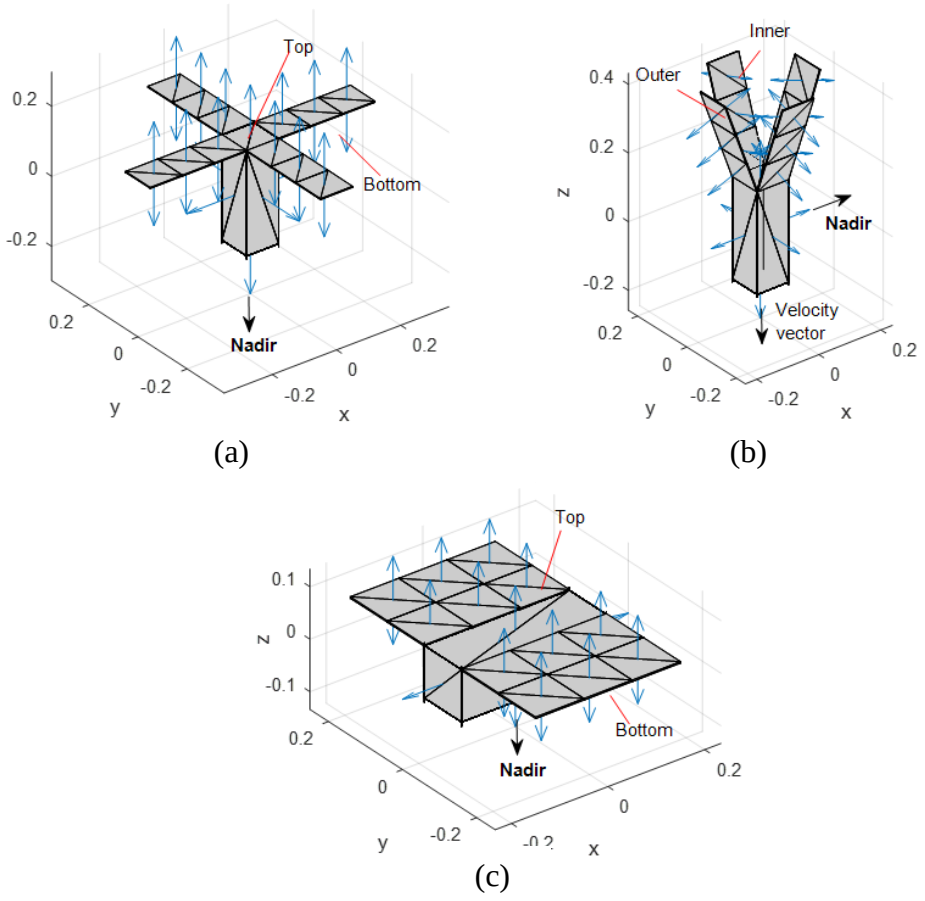

Figure 3-1. CubeSat geometry of (a) Model 1, (b) Model 2, and (c) Model 3 with surface normal indicated by the solid arrows.

simplified model of areas and normal, and consist of a set of vertices and faces defining the exterior of the satellites. The optical property of body surfaces that are mounted with solar cells is assigned as a solar cell, whereas the surfaces that have no solar cells are assigned as radiator surface. All three models can be considered as common designs as they are commercially available [60,74,75] and similar designs were used for some CubeSat missions and studies [4,20,50,70,76,77].

The cube faces have 6 surfaces, which create the satellite body. Each model had four fixed, body-mounted solar panels on the long section surfaces. Each deployable solar panel had a length of 300 mm, a width of 100 mm, and a thickness of 3 mm. Each panel is divided into 3 parts with each part having 2 surfaces: top and bottom. Therefore, each deployable solar array has 6 surfaces that can be defined differently. Altogether, each model has 30 surfaces to be defined. Surface normal vectors are shown by the blue arrows in Figure 3-1. In the simulation code, both areas and surface normal vectors are gathered into their respective matrix and placed into the x-, y-, or z-axis.

For ease of comparison, all the CubeSat models used have the same mission: a nadir-pointing mission. We assumed that their respective attitude control systems are able to maintain the pointing in the directions assigned. The state-of-the-art CubeSat technology has been found to be potentially compatible with some Earth observation missions [3]. For Model 1, the satellite has four deployable solar panels attached 90 degrees at the +z-axis short edges of the satellite body. The top surfaces of the solar panels and four sides of the x-axis and y-axis satellite body are assigned as solar cells, whereas the bottom sides of the extendable panels and z-axis sides of the body are assigned as a radiator. The nadir pointing is on the –z-axis of the satellite body. Model 2 has its extendable solar panels angle deployed at fixed 30 degrees with respect to the +z axis of the satellite. This configuration is normally known as the space-dart configuration. The outer sides of the deployable solar panels are assigned solar cell surface properties, whereas the inner sides are assigned radiator surface properties. The remaining surfaces of the main satellite body part are assigned as Model 1. This configuration was found to be capable in providing attitude aerodynamic stability for CubeSats that orbit at altitudes below 500 km [20,70]. To manipulate the aerodynamic drag for attitude stabilization, the short section of the satellite body that does not have deployable solar panels (in this case, the -z-axis side) point in the direction of the

velocity of the satellite. We set one long section of the body to be fixed to the nadir pointing direction (in this case the +x-axis side) to match the nadir pointing missions of the other two models to facilitate the solar radiation torque comparison study. Lastly, Model 3 has two-double solar panels deployed along the long edge of the 3U CubeSat body. Like Model 1, the top surfaces of the solar panels are solar cells and the bottom sides are radiators. The nadir pointing is also on the –z-axis of the satellite body.

3.3.2 Position of the Sun and Eclipse Condition

To compute the Sun's position with respect to the satellite for any given location at a given time, there are three steps to follow [78]: (1) calculate the Sun's position in the ecliptic coordinate system, (2) convert result from step 1 to the Earth-centred inertial (ECI) frame, and (3) convert result from step 2 to the satellite body coordinate system.

For the first step, a simple algorithm is used to generate the position of the Sun in the ecliptic coordinate system to a precision of about 1 arcminute for dates between 1950 and 2050. First, compute a number of days, *j*, from the epoch referred to as Julian date, 2,451,545.0:

$$j = JD - 2451545.0 \tag{3.9}$$

where JD is the Julian date of interest. Then, the mean longitude of the Sun (L), mean anomaly of the Sun (g), and ecliptic longitude of the sun (λ) are computed:

$$L = 280.460^{\circ} + 0.9856474^{\circ} j \tag{3.10}$$

$$g = 357.528^{\circ} + 0.9856474^{\circ} j \tag{3.11}$$

$$\lambda = L + 1.915^{\circ} \sin g + 0.020^{\circ} \sin 2g \tag{3.12}$$

where all the values are in the range of 0° to 360°. The distance of the Sun from the Earth (u_{sun}) in the unit meter can be approximated as follows:

$$u_{sun} = (1.00014 - 0.01671\, cos\, g - 0.00014\, cos\, 2g) * 149600e3 \tag{3.13}$$

Other than λ, and u_{sun}, another parameter to form a complete position of the sun in the ECI frame is the ecliptic latitude, β. The Sun's ecliptic latitude can be approximated by $\beta = 0$. Next, in step 2, the Sun unit sun vector ($\hat{u}_{sun}$) in the equatorial coordinate system is computed as follows:

$$\hat{u}_{sun} = \begin{bmatrix} cos\,\lambda \\ cos\,\epsilon\, sin\,\lambda \\ sin\,\epsilon\, sin\,\lambda \end{bmatrix} \tag{3.14}$$

where ϵ is the obliquity of the ecliptic, which can be approximated by:

$$\epsilon = 23.439° - 4.00 \times 10^{-7} j \tag{3.15}$$

In step 3, the u_{sun} must be converted to a unit vector from the satellite toward the Sun ($\hat{s}$), to be used in Eq. (3.5). In a later section, this conversion will be explained.

Next, the Sun's distance and its position from the Earth can be used to determine the conditions under which eclipses occur. The problem of calculating the eclipse times of a spacecraft orbiting the Earth has been studied in depth using various methods [72,79–81]. In this work, the existing spherical Earth conical shadow model given by Wertz [72] was used—the atmospheric effects are neglected. We were only concerned about the eclipse seen by objects of negligible sizes, such as satellites. The variables for eclipse geometry are shown in Figure 3-2.

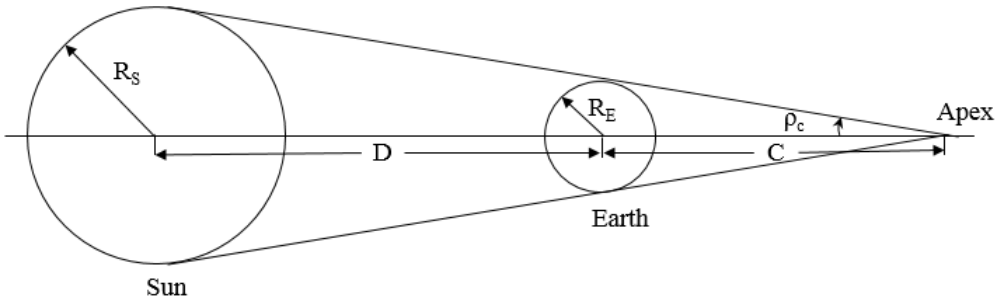

Figure 3-2. Variables for eclipse geometry, where D is the distance from the Earth to the Sun, R_E is the radius of the Earth, and R_S is the radius of the visible surface of the Sun. By simple trigonometry, the distance from the centre of the Earth to the apex of the shadow cone, C=1.385×10^6 km and ρ_c=0.264°.

To find the condition when a satellite is in eclipse condition, let $\vec{D}_S$ be the vector from the satellite to the Sun and let $\vec{D}_E$ be the vector from the satellite to the centre of the Earth. Referring to Figure 3-3, from the satellite's position, the parameters to be determined are the angular radius of the sun, ψ_S, the angular radius of the Earth, ψ_E, and the angular separation, θ, between the Sun and the Earth. These three parameters are given by:

$$\psi_S = \sin^{-1}\frac{R_S}{D_S} \tag{3.16}$$

$$\psi_E = \sin^{-1}\frac{R_E}{D_E} \tag{3.17}$$

$$\theta = \cos^{-1}\left(\hat{D}_S \hat{D}_E\right) \tag{3.18}$$

The necessary conditions for the total eclipse occur when:

$$D < D_S < (D + C) \text{ and } (\psi_E - \psi_S) > \theta \tag{3.19}$$

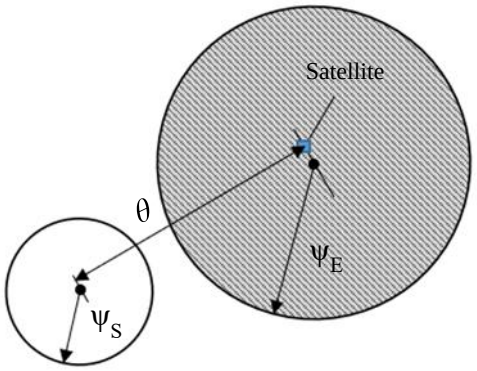

Figure 3-3. Solar eclipse geometry. The parameters to be determined are the angular radius of the Sun, ψ_S, the angular radius of the Earth, ψ_E, and the angular separation θ, between the Sun and the Earth.

3.3.3 Solar Power Calculation

The power produced by the solar arrays mounted on the body and the deployable solar panels for any given location at a given time is [71]:

$$Power = \sum_{i=1}^{16} \eta \rho_a A_i \, Sn_i \hat{s}^T n \quad \text{for } \hat{s}^T n > 0 \tag{3.20}$$

where i is the solar cell number, η is the solar cell efficiency, and $\hat{s}^T n$ is the dot product, equivalent to the cosine of the angle between $\hat{s}$ and n. Whenever the resultant dot product is negative, it means that the particular surface does not face the Sun, and hence does not produce any power. In addition, since the solar cell mounted is normally smaller than the panel area, we set the A value in Eq. (3.20) to 70% of the total panel surface area, for a more realistic result.

3.4 SIMULATION PROGRAM FLOW

The simulation software program was implemented using Princeton Satellite Systems CubeSat Toolbox [82], which is a MATLAB® Toolbox (The MathWorks Inc., Massachusetts, USA) for designing CubeSats and analysing CubeSats missions.

Figure 3-4 shows the flow chart of the simulation software program. Only solar radiation torque computation will be explained since the same procedure is applied to other disturbances albeit with differences in the environment parameters. The first step is to define data for the CubeSat model. Data that are populated consist of the satellite's centre of mass (C_m), deployable solar panels dimension and configuration, surface vectors with respect to the origin ($rFace$), surface area (A), surface of the outward unit normal (n), and the optical properties (ρ) of each surface. In the second step, simulation time is first set as a reference to pre-allocate the maximum amount of space required by arrays of data in the subsequent process. This can improve the code execution time.

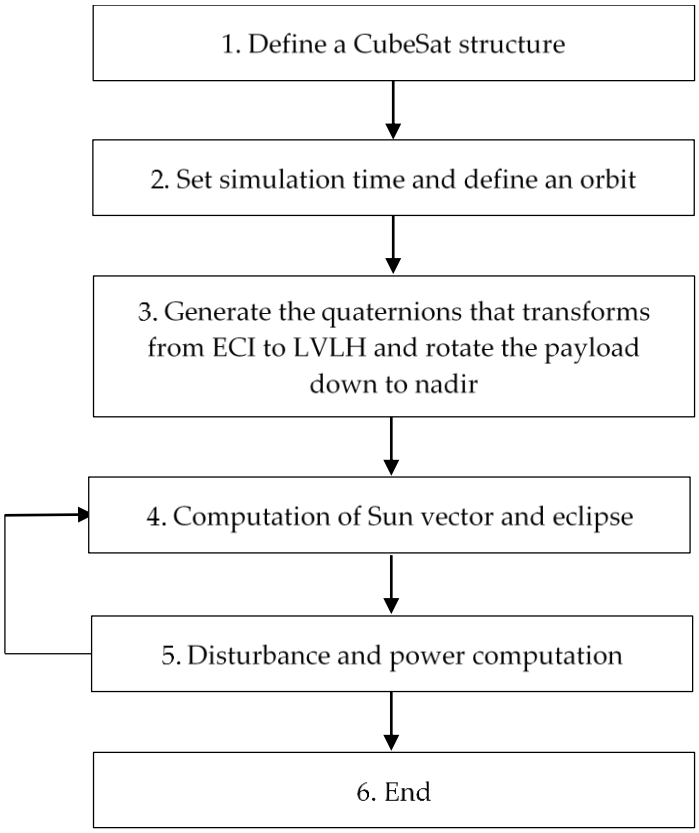

Figure 3-4. Flowchart of disturbance computation

Next, the initial position and velocity vectors of the satellite are propagated based on a defined Keplerian elements. An orbit can be described using six classical Keplerian orbital elements: semi-major axis (a), eccentricity (e), right ascension of the ascending node ($RAAN$), inclination (i), argument of perigee, and mean anomaly. These elements can provide information on the orbit size, orbital plane, and the

position of the satellite. However, it is easier to use Cartesian elements that consist of a position $\vec{r}$ and velocity $\vec{v}$ for propagating the orbit. By using small step sizes, a numerical integrator can determine the new position and the velocity of the satellite given the current position, velocity, and acceleration. Subsequently, acceleration from other forces can be added, such as the solar radiation pressure effect. The Cartesian coordinate frame used in step 2 is the Earth-centred inertial (ECI) coordinate frame, which has its origin at the centre of the Earth and is inertially fixed (Figure 3-5). The fundamental plane contains the equator, and the positive X-axis (X_I) points in the vernal equinox direction. The Z-axis (Z_I) points in the direction of the geographical North Pole and the Y-axis (Y_I) completes the right-hand set of coordinate axes. The algorithm to convert between Kepler elements to Cartesian elements are well documented, for example by Wertz [72] and Sidi [83].

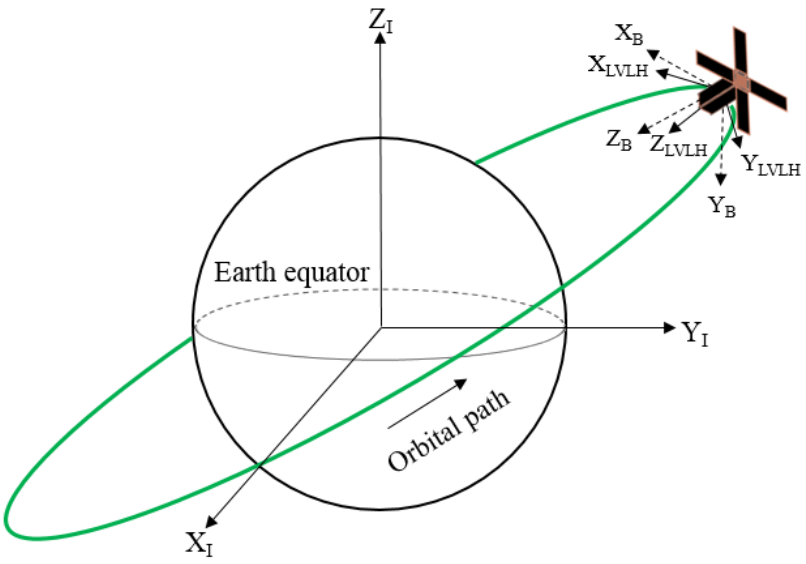

Figure 3-5. Coordinate frames for nadir-pointing satellite.

Although the simulator is able to consider various orbital parameters, some simplifications can be applied when studying the solar radiation torque in LEO. Firstly, since the amount of momentum flux that is incident on an earth-orbiting satellite is roughly the same within the earth's vicinity (i.e., at 1 astronomical unit) [69], the altitude or the semi-major axis can be fixed at one value. Then, the focus is on the shape of the disturbance during the transition from eclipse to daylight and vice versa.

The rapid changes in thermal loading initiated during the transitions have been known to cause thermally induced dynamics in satellite appendages such as the deployable solar arrays [42,47,84]. Therefore, a class of orbits can be selected, such as the orbit occupied by the ISS. The orbit is essentially important for CubeSats since, from 2012 to 2018, more than 200 CubeSats have been launched from ISS, mainly through services provided by the Japan Aerospace Exploration Agency (JAXA) [85] and the National Aeronautics and Space Administration (NASA) [86]. Next, a circular orbit is assumed; therefore, eccentricity is always zero and the argument of perigee can be removed. This is sensible since most satellites in LEO have an eccentricity less than 0.01 [4]. The inclination (*i*) and *RAAN* define the orbit plane, which means that the sun angle to the satellite depends on them. Therefore, the values of *i* and *RAAN* vary throughout the simulations.

In the third step, the satellite is aligned to the local vertical local horizontal (LVLH) coordinate frame from the ECI frame. The LVLH is another coordinate frame that has its origin at the centre of the satellite and fixes to the orbit (Figure 3-5). It is commonly assigned to Earth/nadir-pointing satellites, where Z_{LVLH} points towards the Earth, Y_{LVLH} is normal to the local plane with a negative direction, and X_{LVLH} completes the right-handed orthogonal axis set. By completing the transformation from ECI to LVLH, the motion of the satellite can be described by the translational motion of the centre of mass of the satellite around the centre of the mass of the Earth. The transformation from ECI to LVLH can be performed following the procedure outlined by Paluszek et al. [71]. Let the ECI unit vector be $\hat{u}_I$, and let $[\quad]_u$ represent the unit operator on a vector, returning a vector of the same direction with length 1:

$$\hat{u}_I = M^T \hat{u}_{LVLH} \tag{3.21}$$

where M is a transformation matrix used to transform vectors from the ECI frame to LVLH frame and $\hat{u}_{LVLH}$ is a unit vector defined in the LVLH frame.

The transformation matrix M may be computed from the spacecraft ECI position ($\vec{r}$) and velocity ($\vec{v}$) vectors as follows:

$$M = \begin{bmatrix} x^T \\ y^T \\ z^T \end{bmatrix} \tag{3.22}$$

where $y = [\vec{v} \times \vec{r}]_u$, $z = -[\vec{r}]_u$, and $x = [y \times z]_u$. The transformation matrix above has nine elements which complicate its application for the propagation of an object. A more efficient method involves using quaternion terminology, which has a mere four elements. The quaternion (in this case the quaternion from ECI to LVLH frame) is represented by a four-row vector:

$$q_{I/LVLH} = \begin{bmatrix} q_0 \\ q_1 \\ q_2 \\ q_3 \end{bmatrix} = q_0 + iq_1 + jq_2 + kq_3 \tag{3.23}$$

where q_0 is a scalar component and q_{1-3} are vector components. The conversion of the transformation matrix to quaternion can be obtained using the procedure outlined by Sidi [83].

Next, we wanted to rotate the payload down to the nadir direction. As an example, for Model 1 CubeSat, the nadir pointing is at the –z-axis. The pointing target vector can be achieved by rotating the CubeSat 180° around the x-axis. The quaternion of this rotation (from LVLH coordinate frame to body coordinate frame), herewith named $q_{LVLH/B}$, is:

$$q_{LVLH/B} = cos\,\theta + i(x\,sin\,\theta) + j(y\,sin\,\theta) + k(z\,sin\,\theta) \tag{3.24}$$

where θ is the angle of rotation and x, y, and z are vectors representing the rotation axes. Finally, the transformation from the ECI frame to body frame can be obtained as follows:

$$q_{I/B} = q_{I/LVLH} q_{LVLH/B} \tag{3.25}$$

From here on, each set quaternion and its correspondence time and other properties defined in the first step are processed one at a time in the fourth and fifth steps.

In step 4, the Sun distance, its unit vector in the ECI frame, and the position when the satellite is in daylight or eclipse are computed using the methods explained in Section 3.2. In the last step, solar pressure force due to the solar flux from the Sun, albedo, and Earth-emitted radiation in the satellite body frame are collected, and then the disturbance torques are calculated. For the surfaces that face the solar flux, to find the unit sun vector $\hat{s}$ in Eq. (3.5), the unit sun vector $\hat{u}_{sun}$ obtained in Eq. (3.13) must be converted to the unit vector from the satellite toward the Sun. This can be completed using quaternion transformation as follows:

$$\hat{s} = q_{I/B}\hat{u}_{sun}q_{I/B}^{*} \tag{3.26}$$

where $q_{I/B}^{*}$ is the conjugate of $q_{I/B}$. For the surface not facing the sun, the $\hat{s}$ is replaced as follows:

$$\hat{s} = q_{I/B}(-[\vec{r}]_u)q_{I/B}^{*} \tag{3.27}$$

The value of $\hat{s}$ in Eq. (3.26) will be used in solar flux force and solar power calculations, whereas the value of $\hat{s}$ in Eq. (3.27) will be used for both albedo force and Earth-emitted radiation force calculation. The negative sign in Eq. (3.27) indicates that the source of radiation is from the nadir direction. The total force on the satellite body $\vec{F}_B$ will be the summation of these three forces. The eclipse condition determined in the fourth step is also considered during the calculation. The force on a surface acts as a torque on the satellite body if the face is offset from the centre of mass, as:

$$\vec{T} = \sum(\overrightarrow{rFace - C_m}) \times \overrightarrow{F_B} \tag{3.28}$$

3.5 DISTURBANCE AND POWER EVALUATION

A series of simulations were conducted to evaluate the solar radiation disturbance on the CubeSat models in LEO. The data of this orbit are shown in Table 3-1. The orbit used resembles the orbit occupied by the ISS. The simulation time was set to one year to demonstrate the effects of season change. One year is a reasonable period since most CubeSats are currently designated with a mission lifetime less than one year long. The orbital parameters were simplified to focus solely on the characteristics of solar radiation torque. Therefore, the variation in inclination from 0 to 90 degrees is shown to demonstrate the variation in solar radiation torque due to satellite orientation with respect to the Sun. The fluctuation range of the disturbance torques between positive and negative values are used to compare performance among the models tested. Additionally, the solar power generation of the different configurations was compared. Details of the satellite specifications and disturbance parameters are provided in Tables 3-2 and 3-3.

The simulation time of the six orbits of eclipse fraction at 408 km altitude is depicted in Figure 3-6. In each orbit period, the eclipse fraction lasts about 2180 s, whereas the remaining daylight period lasts around 3352 s. Accordingly, the fraction of solar flux follows suit (i.e., occurs only during the daylight period). As shown in

Figure 3-6, the Earth-emitted radiation is constant throughout the orbit, since we previously assumed that it is uniform over the surface of the earth, whereas the reflected radiation due to albedo varies with the sun vector and satellite vector from the Earth.

Table 3-1. Orbital parameters

Parameter	Value
Semi major axis (a)	408 km
Orbit inclination (i)	51.64°
Initial right ascension of the ascending node (RAAN)	0°
Argument of perigee (ω)	0°
Eccentricity (e)	0
Initial mean anomaly (M)	0°
Initial Julian date	2,458,563

Table 3-2. CubeSats Specification

Item	Specification	Value
All three models	Center of mass (x, y, z)	(0, 0, 0)
	Residual dipole (x, y, z)	(0, 0, 0.002 Am^2)
Solar cell surface properties [82]	Absorbed (ρ_a)	0.75
	Diffuse (ρ_d)	0.08
	Specular (ρ_s)	0.17
Radiator surface properties [82]	Absorbed (ρ_a)	0.15
	Diffuse (ρ_d)	0.16
	Specular (ρ_s)	0.69

Table 3-3. Disturbance parameters

Parameter	Value
Solar flux (S)	1367 Wm^{-2}
Earth radiation	400 Wm^{-2}
Albedo factor (aF)	0.33
Atmospheric density (ρ_{atm})	3.725E-12 kg/m^3
Drag coefficient C_D	2

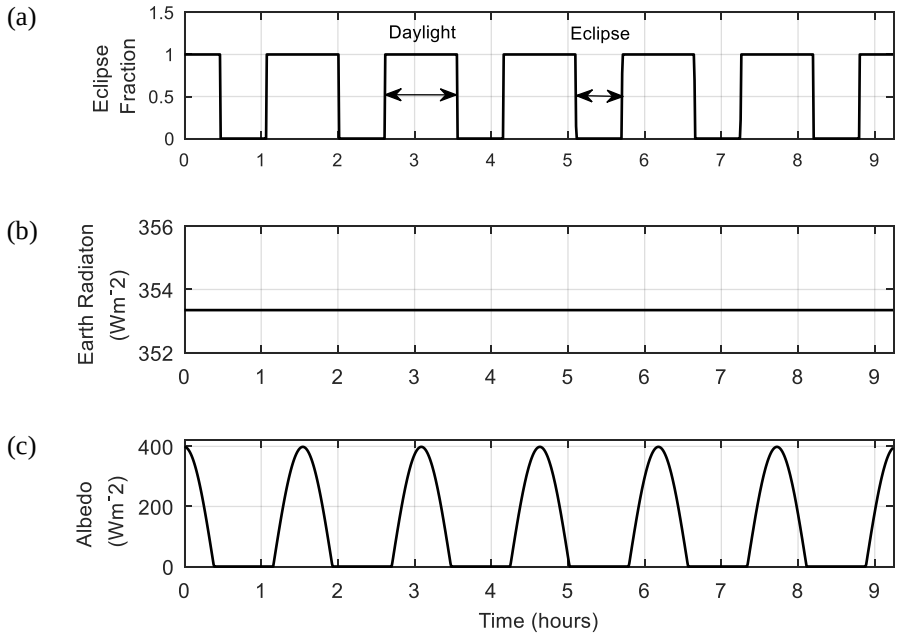

Figure 3-6. (a) Eclipse fractions, (b) earth radiation, and (c) radiation due to albedo at 408 km altitude.

3.5.1 Solar Radiation Torque in Model 1

The simulation results of the solar radiation torque in Model 1 in the x-axis (T_x) and y-axis (T_y) are presented in Figure 3-7. The results show the one-year orbit period with the start of seasons indicated, whereas sub-figures provide more detailed disturbance characteristic of six orbits' simulation time. At the inclination set, the *RAAN* varies over 360° in a one-year simulation. There is no net torque in the z-axis (T_z), since the deployable solar panels form a symmetric satellite configuration with respect to the solar forces acting on it. Differences in the disturbance torque level due to seasonal effects can be seen as the Earth's axis tilts with respect to the Sun's rays changing. These effects are more apparent on T_x than T_y. During the summer solstice and winter solstice, the T_x is at a maximum and drops to almost zero during the autumnal equinox and vernal equinox. T_y registers its maximum and minimum in opposite seasons. Figure 3-7(a) shows the level of T_x during the summer solstice. The disturbance is mainly caused by the solar flux pressure on the deployable solar panels as they face the Sun throughout the daylight period. The level slowly increases when the satellite leaves the eclipse, and reaches its peak when the satellite passes through the equatorial line and subsequently declining until it enters the eclipse. However, the more concerning characteristic is the sudden torque increase and decrease at the edge of the eclipse, since the rapid change in the disturbance torque might cause sudden

rotational motion of the satellite. For this particular case, the condition occurs because when the satellite is in the transition from eclipse to daylight and vice versa, two different sides exchange positions to face the solar flux from the Sun. For example, when the satellite emerges from eclipse, the solar flux first hits the solar cell surface on its body for a while before the deployable solar panels face the Sun. Figure 3-7(b) shows the level of T_y during autumnal equinox, at which the T_y is at maximum. As in T_x, sudden torque changes can be seen during eclipse transitions. During the day, T_y has two peaks due to differences in the position vector of the Sun when the satellite is in the southern and northern hemispheres of the Earth.

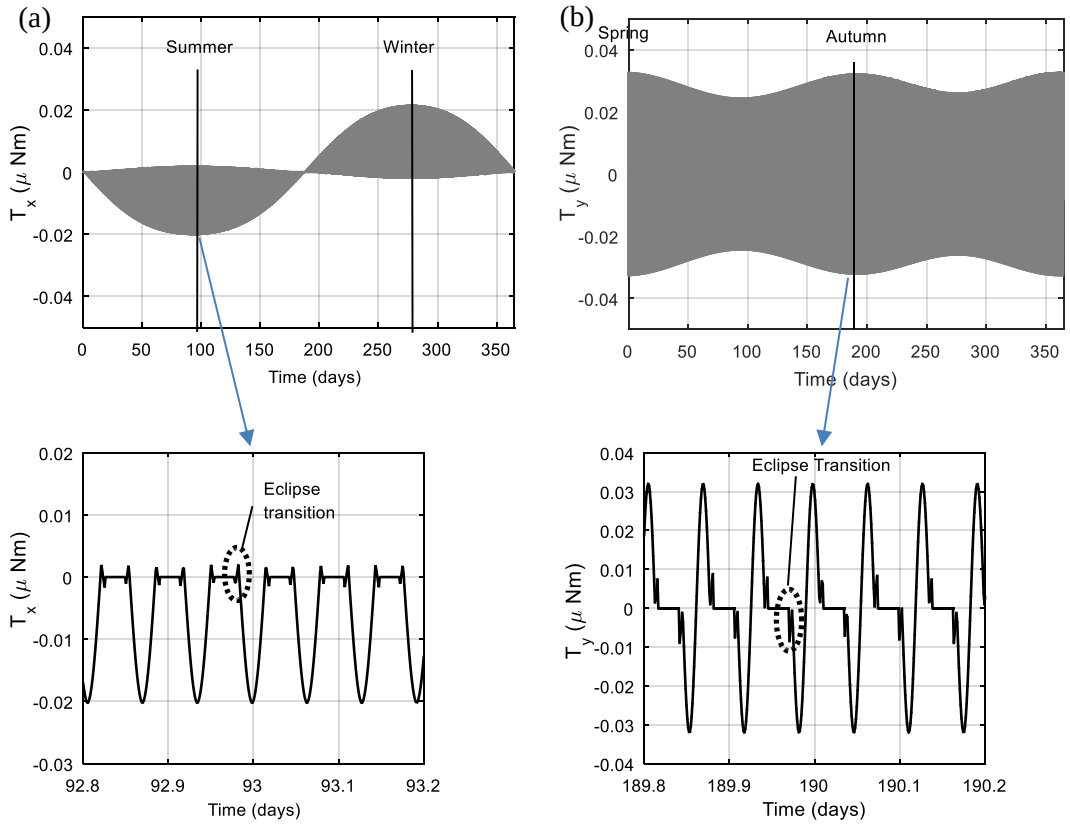

Figure 3-7. Solar radiation torques in Model 1 in the International Space Station (ISS) orbit for one-year simulation and six orbit periods at seasonal start time: (a) T_x and (b) T_y.

Next, the shapes of solar radiation torques with inclination angles varying from 0° to 90° are depicted in the three-dimensional (3D) plots of Figure 3-8. Each plot is an orbit long simulation taken during the summer solstice. The surface plots show the time and angle at which the torque magnitudes are among the maximum at their respective axes. In Figure 3-8(a), the T_x changes direction at the inclination of 23.4° due to the Earth's obliquity. The maximum T_x occurs in the region when the inclination is around 70°. The shape of T_y with varying inclination angles is shown in Figure 3-

8(b). The overall shape of the plot is basically the same regardless of the inclination, but the levels differ accordingly. From the 0° inclination, its maximum level increases until the highest, which occurs when the inclination is 23.4°, then subsequently declining almost linearly with increased inclination.

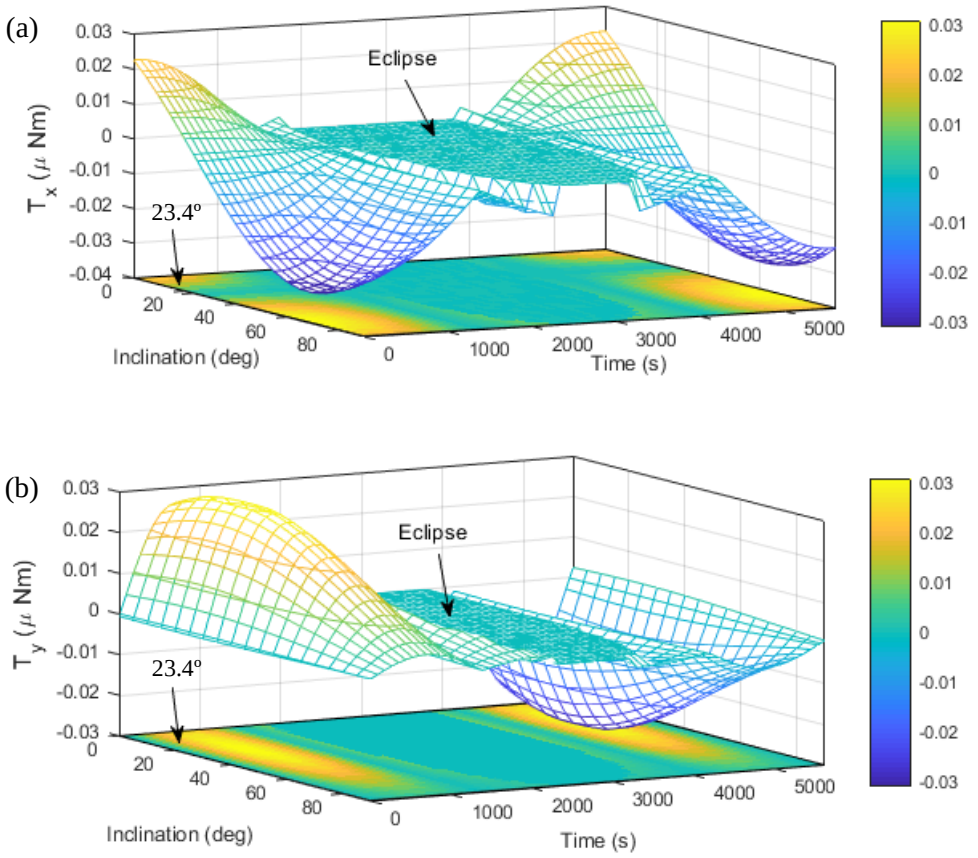

Figure 3-8. One orbit period of solar radiation torques in Model 1 in ISS orbit with varying inclination angles. (a) T_x and (b) T_y.

3.5.2 Solar Radiation Torque in Model 2

The simulation results of the solar radiation torque in Model 2 are presented in Figure 3-9. The shape of the one-year long simulation T_x is the opposite of Model 1, whereas T_y, similar to Model 1, always fluctuates between positive and negative torques throughout the orbit. Compared to Model 1, the fluctuation range of T_x and T_y increased by 134% and 108%, respectively. The sub-figures detailing the shape of the torques in the six orbit periods further reveal the differences in comparison to Model 1. The torques produced during the eclipse transitions look rather smooth compared to those in Model 1, which occurred due to differences in the solar panel configurations

and the satellite's velocity direction, although the vector direction of the Sun to the Model 2 satellite is different, resulting in the occurrence of T_z as well, where the order of magnitude is 10 times lower than T_x.

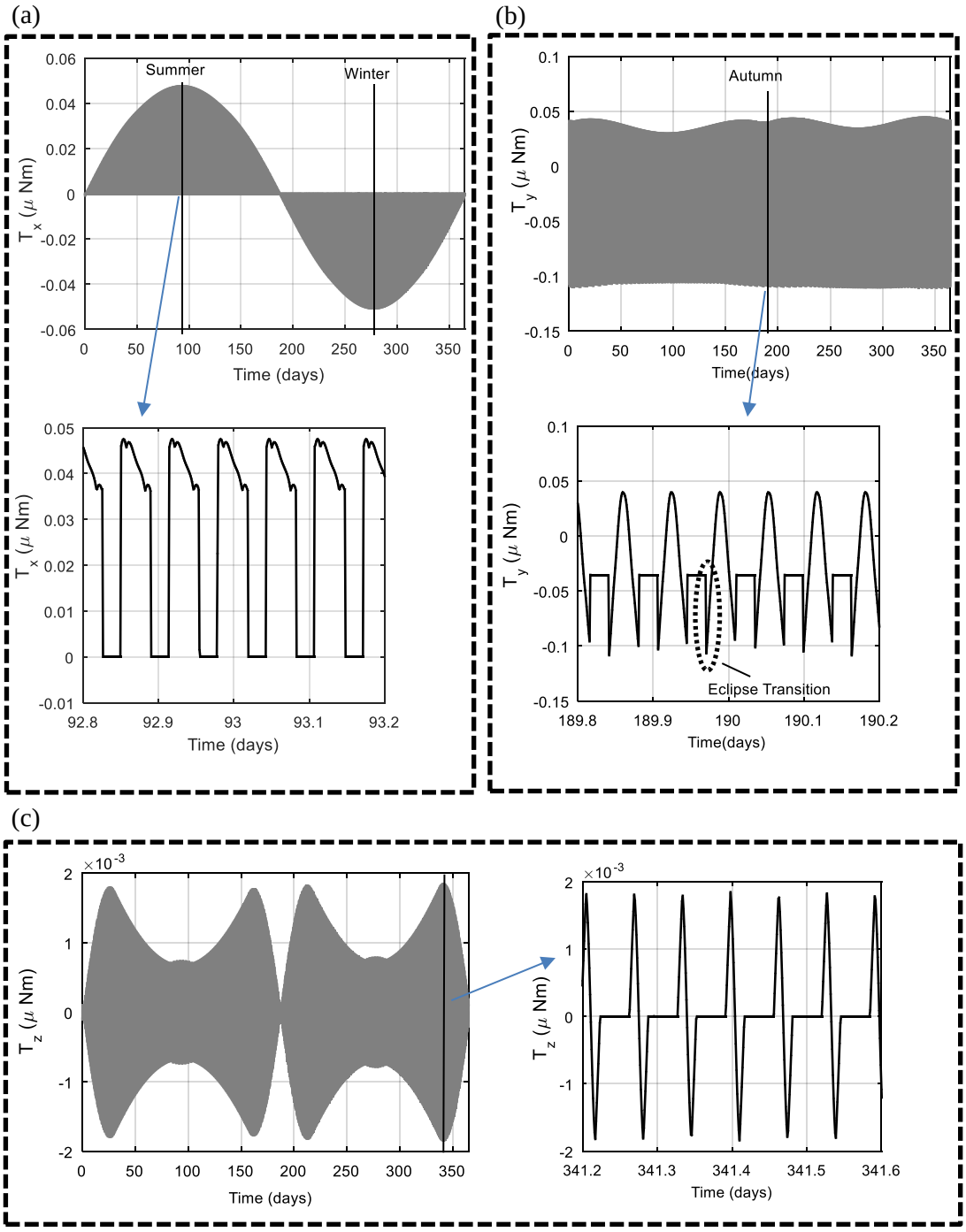

Figure 3-9. Solar radiation torques in Model 2 in ISS orbit for one-year simulation and six orbit periods at seasonal start time: (a) T_x, (b) T_y, and (c) T_z.

From the 3D torque plots during the summer solstice in Figure 3-10, the inclination angles would be a factor of the level of T_x. The higher the inclination, the higher the magnitude of T_x. For T_y, regardless of the inclination angle, maximum levels

always occur during eclipse transitions. The effects of inclination angle change can also be observed in the pattern of T_z. Four peaks occur in high inclination but only two peaks in low and mid inclinations.

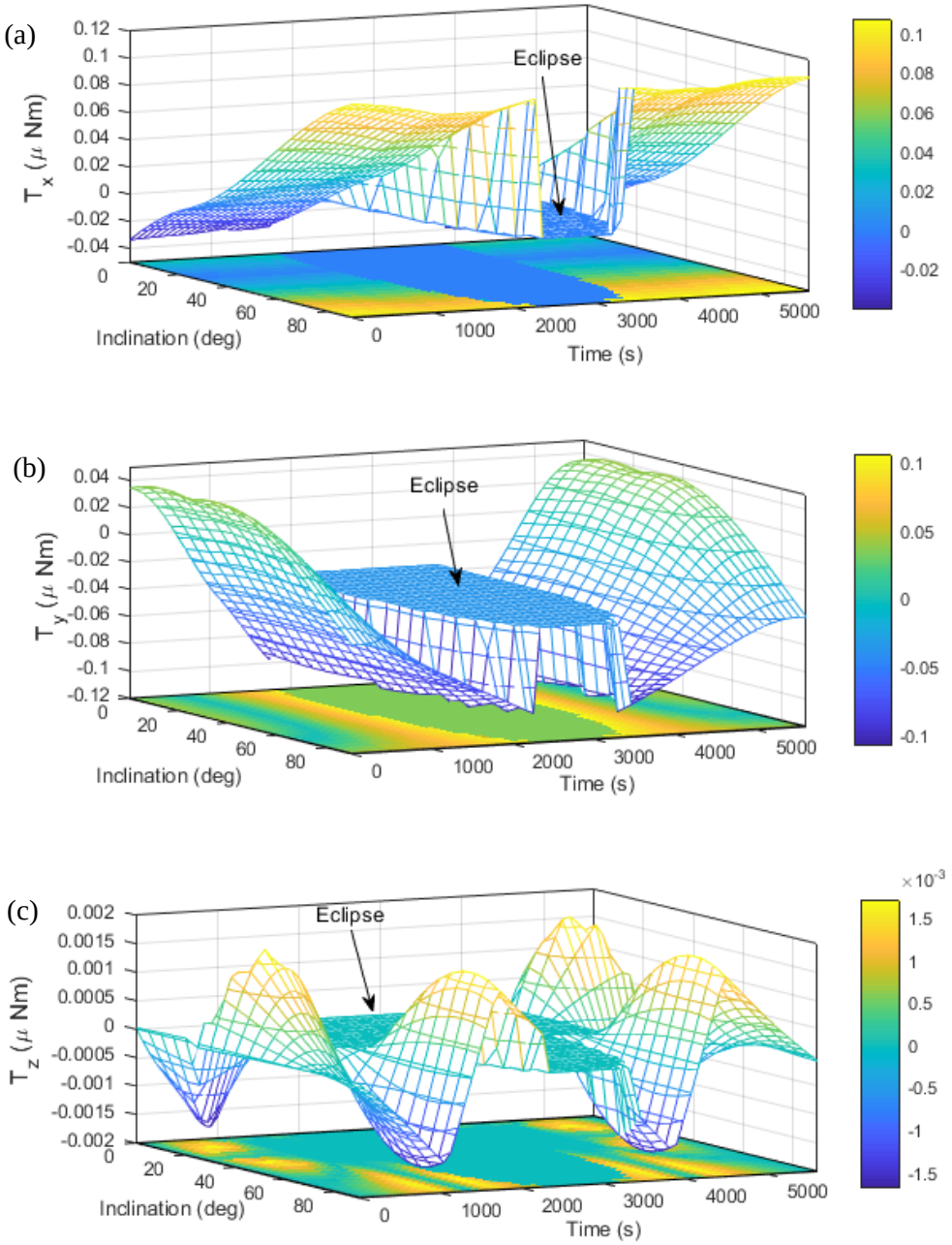

Figure 3-10. One orbit period of solar radiation torques in Model 2 in ISS orbit with varying inclination angles: (a) T_x, (b) T_y, and (c) T_z

3.5.3 Solar Radiation Torque in Model 3

The simulation results of the solar radiation torque in Model 3 are presented in Figure 3-11. The shapes of solar radiation torques, taken during the summer solstice

with inclination varying from 0° to 90° are depicted in 3D plots in Figure 3-12. As expected, results of Model 3 are similar to those of Model 1 because the vector direction of the Sun to the deployable solar panels and the pointing mission are similar to Model 1. The main difference is the lower peak torques in both T_x and T_y. This was expected since the distances between solar panels and the satellite body of Model 3 are shorter than in Model 1. Compared to Model 1, the fluctuation ranges of T_x and T_y decreased by 62 and 70%, respectively.

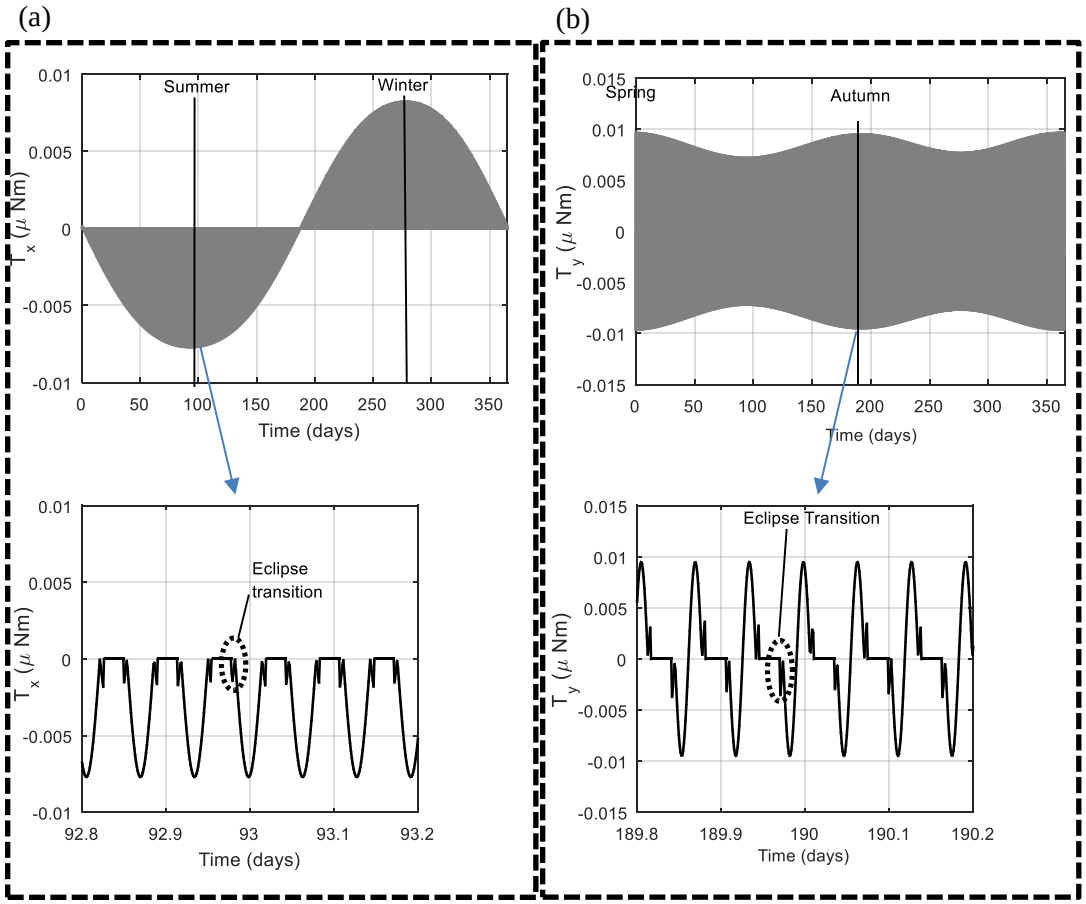

Figure 3-11. Solar radiation torques in Model 3 in ISS orbit for one-year simulation and six orbit periods at seasonal start time: (a) Tx and (b) Ty.

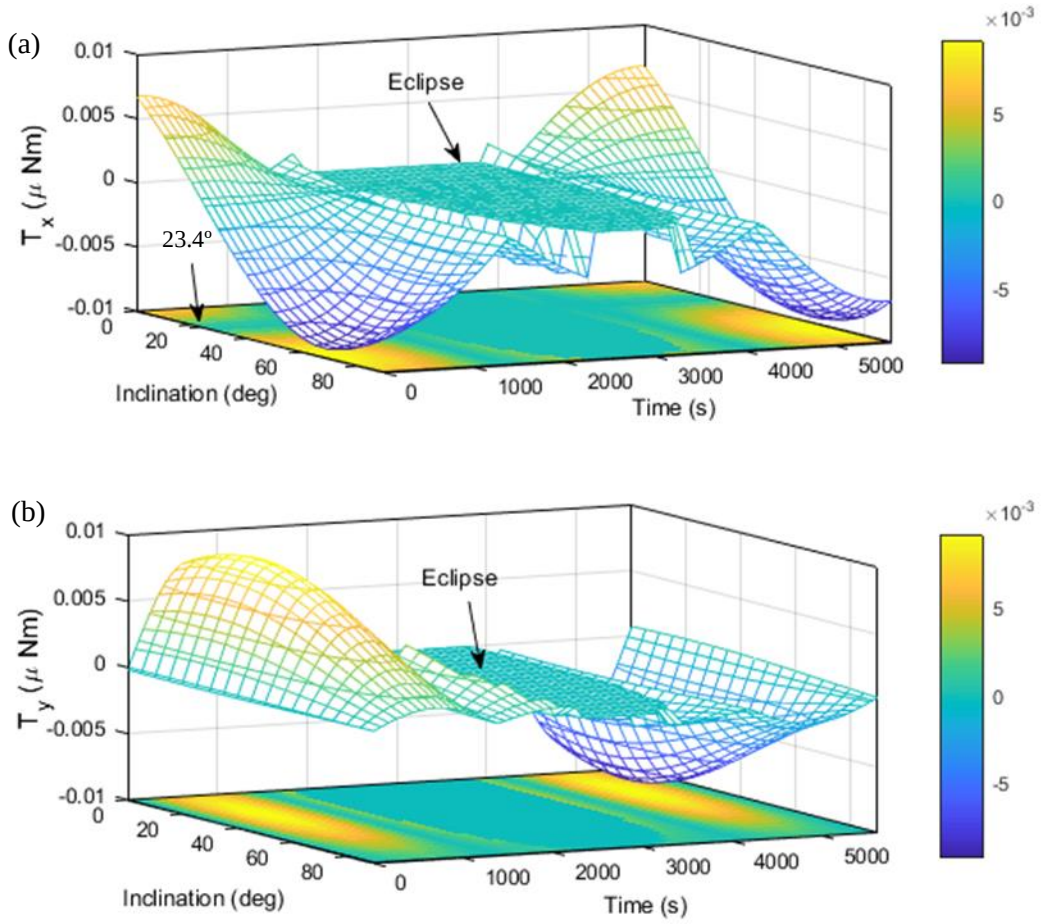

Figure 3-12. One orbit period of solar radiation torques in Model 3 in ISS orbit with varying inclination angles: (a) Tx and (b) Ty.

3.5.4 Solar Power Generation

The simulation results of the solar power generation in Models 1, 2, and 3 over a one-year orbit period are presented in Figure 3-13. The sub-figures for the six orbits' simulation times, taken during the summer solstice, provide a more detailed plot of the generated power. Seasonal effects can be seen affecting the peak level of the power generated. As expected, Models 1 and 3 have similar shapes since the solar radiation torques over the one-year period are similar. For Model 1, the peak power is 25.2 W and the average power is 10.4 W. Model 2 has the lowest peak power and average power at 16.26 W and 6.1 W, respectively. Model 3 has the highest peak power at 30.3 W. However, its average power, at 9.9 W, is lower than that of Model 1.

The use of deployable solar panels has significantly improved power generation, especially for Models 1 and 3. Considering the same nadir-pointing missions specified, when compared with their respective configurations without deployable solar panels,

Model 1 performs 201% better, whereas Model 3 achieves a 237% increase in average power. Model 2 produces around a 107.4% improvement.

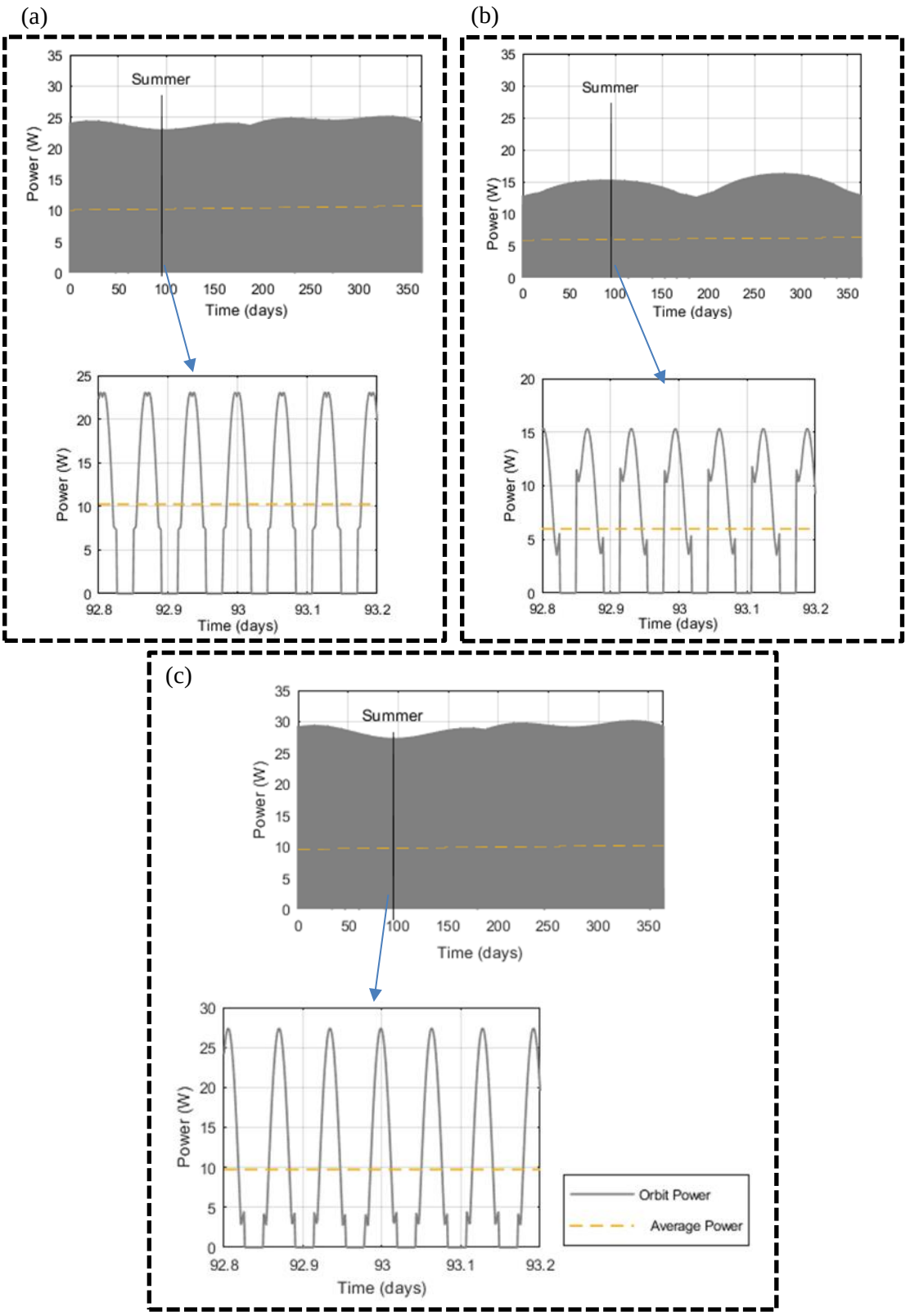

Figure 3-13. Solar power generation over 1-year period of (a) Model 1, (b) Model 2, and (c) Model 3.

3.5.5 Discussion – Effects of Adding Deployable Solar Panels on the Overall Disturbances

From the initial results above, characteristics of solar radiation torque of each CubeSat configurations were obtained. By including other external disturbances to those results, the effects of adding the deployable solar panels on the total external torques can be better observed. While the total resultant torques presented by no means the maximum torques that will be experienced by the satellites, especially since initial condition after deployment is not considered, forecast on the maximum resultant torques to maintain the nadir-pointing mission proposed would very useful for design engineers to plan overall power usage. One-year long period results of total torque in ISS orbit for Model 1, Model 2 and Model 3 are plotted in Figure 14, Figure 15 and Figure 16 respectively. In each figure, comparison between the total torque with deployable solar panels and with none are made. Although not shown separately, the type of disturbance which dominates the total torque will be explained.

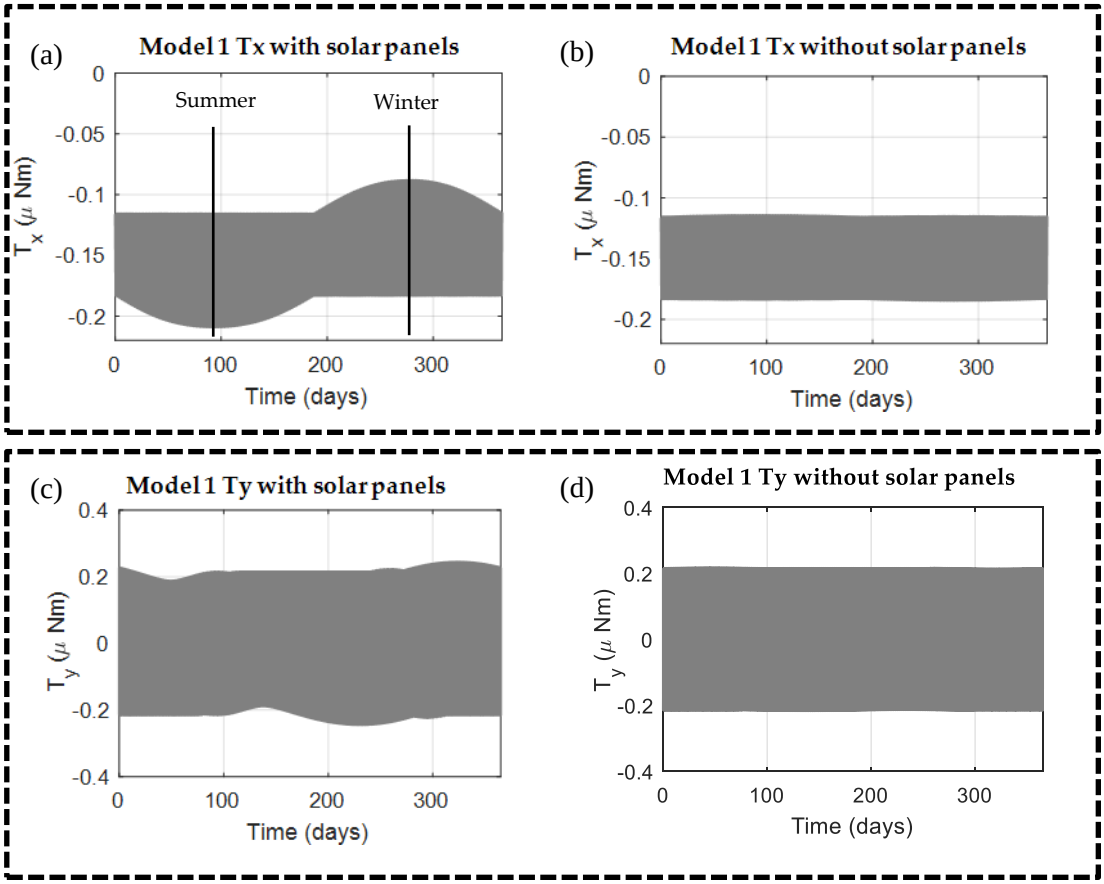

Figure 3-14. Total disturbance torque in Model 1 in ISS orbit over 1-year simulation period. (a) Tx with solar panels, (b) Tx without solar panels, (c) Ty with solar panels, and (d) Ty without solar panels.

Firstly, the resultant T_z for each model is not presented since the value is negligible compared to T_x and T_y. For Model 1, the total torques are mainly contributed by the satellite's residual dipoles. Due to the nadir-pointing mission chosen and the model's configuration, both the gravity gradient torque and the aerodynamic torque are negligible. However, solar radiation torque contribution is still obvious especially in the x-axis, as shown in Figure 3-14(a). At the maximum, for example, during the summer solstice, the increase of disturbance torque is about 13.3% for T_x and 12.7% for T_y when compared to not using the solar panels.

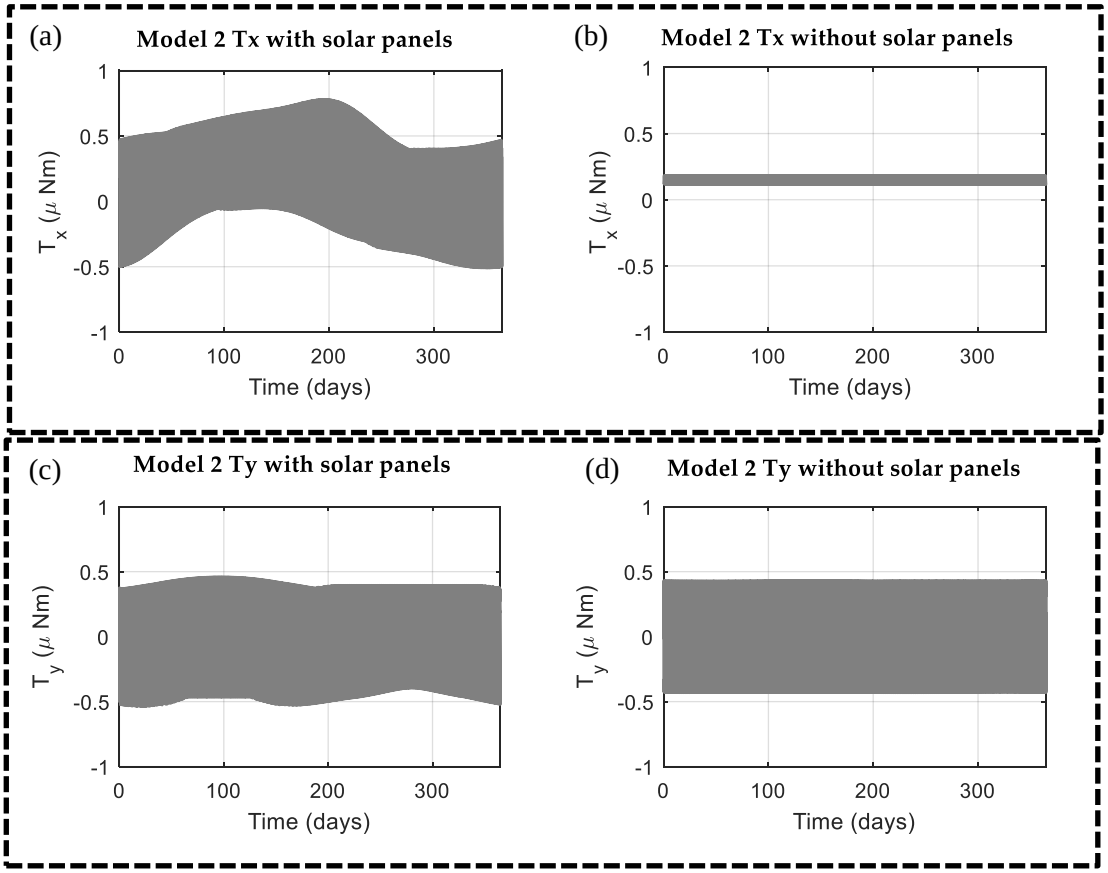

Figure 3-15. Total disturbance torque in Model 2 in ISS orbit over 1-year simulation period. (a) Tx with solar panels, (b) Tx without solar panels, (c) Ty with solar panels, (d) Ty without solar panels.

Next, for Model 2, a significant increase of total torque in x-axis can be seen in Figure 3-15(a) when the deployable solar panels are mounted. This is mainly contributed by the aerodynamics drag as the space dart configuration contributes to a higher projected area with respect to the velocity direction. At the maximum, the increase of disturbance torque is about 322.6% T_x for and 6.5% for T_y when compared to not using the solar panels. Meanwhile, referring to the plot in Figure 3-9(a), the solar radiation torque is less than 6% of the total disturbance torque.

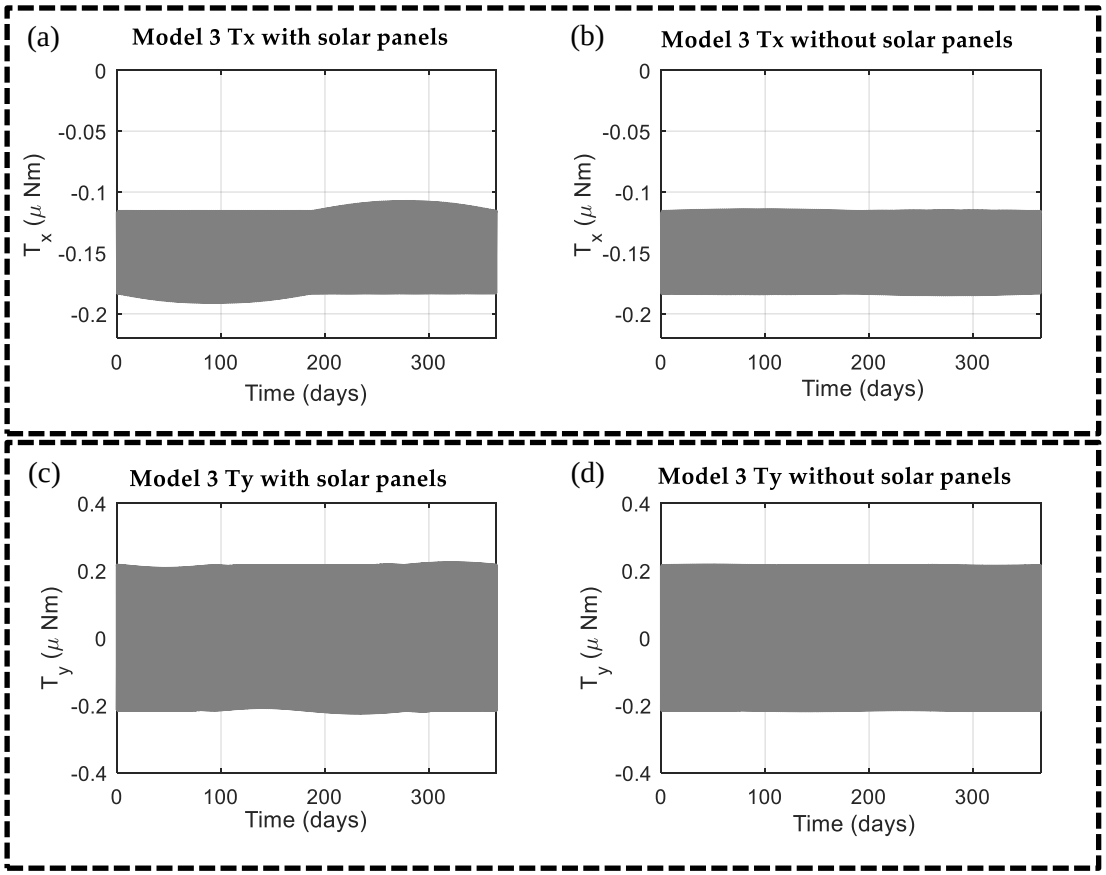

Figure 3-3. Total disturbance torque in Model 3 in ISS orbit over 1-year simulation period. (a) Tx with solar panels, (b) Tx without solar panels, (c) Ty with solar panels, (d) Ty without solar panels.

Lastly, for Model 3, the characteristics are similar to Model 1 albeit with lower total torques in both x-axis and y-axis. As shown in Figure 3-16, at the maximum, the increase of disturbance torque is about 3.4% for T_x and 3.2% for T_y when compared to not using the solar panels.

The data obtained above show that the solar radiation torque produced due to the usage of deployable solar panels are still much smaller compared to other disturbances. The proportion should be much lower if the nadir pointing mission is not used and the satellite's centre of mass is not exactly at the centre of the body. On the other hand, the solar radiation torque proportion will increase when higher altitude is used. Therefore, future work may include these variables to enable better selection of panels configuration.

3.6 CONCLUSIONS

In this study, we examined the solar radiation torques encountered by low earth orbiting nanosatellites with deployable solar panels. The solar power generated when using different configurations of deployable solar panels were presented. The software algorithm used to simulate the disturbance torque and solar power generation was described in detail. The optical properties of different surfaces were distinguished and pointing missions from previous literature were considered when deciding the satellite pointing missions. For demonstration and comparison purposes, three common configurations of 3U-sized CubeSat with deployable solar panels were tested in the orbit occupied by the ISS. The first CubeSat has four deployable solar panels attached 90 degrees at the short edges (Model 1), the second CubeSat resembles the space-dart configuration (Model 2), and the third CubeSat has two-doubled solar panels deployed along the long edge of its body (Model 3). With respect to the nadir-pointing missions defined, Models 1 and 3 would be affected by the eclipse effect in the form of sudden torque increases and decreases. However, Model 1 experiences higher peak radiation torques than Model 3. For Model 2, although not affected by the eclipse transition effect, the overall torque magnitudes are relatively higher compared to those in Models 1 and 3. In terms of average solar power generation, Model 1 leads, followed by Model 3 with just 5% less than Model 1, and Model 3 lags far behind, generating just 59% of the power of Model 1. When compared with other external disturbances, the solar radiation torques produced are within 3.2% to 13.3% of the total torques. Model 1 and Model 3 experience the residual dipole torque the most while Model 2 experience aerodynamic drag the most.

Overall, the solar radiation torque and solar power generation data presented would help CubeSats developers to select the right deployable solar panel configuration for their respective missions. Based on two factors, solar radiation torque, and solar power generation, the Model 3 configuration would be the best option for nadir-pointing missions. Future work will extend the impact of the solar radiation torque on the dynamics of the respective CubeSat models used in the study, as well as the required control torque to maintain the proposed nadir pointing mission.

Chapter 4: Conclusions and Future Work

To furnish diverse studies on the deployable solar panels of the nanosatellite, this dissertation presents a TID analysis and a solar radiation torque study on various configurations of the panel. In this final chapter, the research work is summarized and conclusions are drawn to provide CubeSat designers the capacity to rectify or improve issues with in-orbit disturbances due to the use of the deployable solar panels. Furthermore, potential future directions of research are outlined to improve results of objective functions and to evaluate the satisfaction on mission requirements.

4.1 CONCLUSIONS

The nanosatellite related research has numerous participants; therefore, it is worthy to separate the study which regarded the TID problem, especially since the materials used are different compared to the ones highlighted in available literature. Regarding the content, it is recommended that the procedure for checking the TID problem should start from the thermal analysis until its effect on the satellite body has been ascertained i.e. the combination of thermal analysis to FEA on the quasi-static and thermal snap, as well as inertia relief method for displacement check, due to TID. In the thermal analysis, the possibility of obtaining a different level of temperature, even with identical solar panels used on the CubeSat, is presented. Whereas in the FEA, it is estimated that the disturbance level would be informative toward relevant readers to decide whether the level is worthy of attention (or otherwise) when working on CubeSat missions.

Meanwhile, the solar radiation pressure torque study on CubeSats in LEO has never been covered explicitly, since major disturbances on a particular orbit are mainly contributed by gravity gradient, aerodynamic force, and the Earth's magnetic field. The solar radiation torque is normally treated as a constant value, estimated by the combination of highest possible value of solar flux and the surface area facing the Sun. Therefore, this research sheds detail into the order of magnitude motions that an attitude control system may require, for the purpose of alleviating any occurrence during the use of deployable solar panels. Although the applied numerical simulation was based on a well-established methodology, details were provided in the form of

different surface optical properties and various orbital parameters. The latter provides a better observation into the full coverage of seasonal effects.

4.2 FUTURE WORK

For the TID analysis, since a nanosatellite has a short average operational lifetime, it is noteworthy that the material properties used in this study are assumed to be undegraded from exposure to the space environment, as well as from facilities, and cost constraints. Therefore, to increase the accuracy of the results, the degradation processes on the materials require examination, since they can influence the value rate of temperature fluctuations, as well as the frequency of temperature fluctuations. Furthermore, it might be necessary to discuss contact conditions between layers explicitly. Considering big differences in CTE for particular layers, thermal deformations may induce interlaminar cracking. Regarding the attitude dynamics, the research does not attempt to develop dynamic equations of motion for deployable solar panels. That is because Boyle's parameter value [64] for the structure determines that the thermal loading will not cause vibration problems to the solar panels during an eclipse transition. Further initial checking can also be done using the dynamic equation in earlier literature like Thornton's [39,42,43]. The current research has decided to continue using 3D models for consistency in finding the pointing error displacement with the inertia relief method. However, with wider and longer panels, the control structure interactions might have significant contributions of spatial motion into time constrained motion. It would be interesting to know how the small form factor of CubeSats would behave when such equations are developed and studied.

Meanwhile, for the solar radiation torque study, as shown by the results obtained, the use of different deployable solar panels configurations will certainly yield a difference in the solar radiation pattern faced and the amount of solar power generated. A further advancement would be a discussion pertaining to the effect of the radiation torques on the dynamics of the satellite i.e. for which operative modes (e.g. fine pointing) and/or types of manoeuvre (e.g. quick/slow slew manoeuvres) this torque can affect the operativity of the entire attitude control system. All in all, although actual thermal load on the system is still needed to confirm the accuracy of the results obtained, the numerical simulation methods presented in this research are applicable to estimate functional disturbance on any CubeSat with deployable solar panels. The

results obtained so far can be used as a guide to choose the most appropriate deployable solar panel configuration and to design a better attitude control system for the CubeSat.

References

1. Swartwout, M., The first one hundred CubeSats : A statistical look. J. Small Satell., 2 (2013) 213–233.

2. Space, B.; Metro, D.C.; London, C., Smallsats by the Numbers. (2019). http://brycetech.com/reports.html (accessed July 6, 2019).

3. Selva, D.; Krejci, D., A survey and assessment of the capabilities of Cubesats for Earth observation. Acta Astronaut., 74 (2012) 50–68.

4. Young, D.; Cutler, J.W.; Mancewicz, J.; Ridley, A.J., Maximizing photovoltaic power generation of a space-dart configured satellite. Acta Astronaut., 111 (2015) 283–299.

5. Santoni, F.; Piergentili, F.; Donati, S.; Perelli, M.; Negri, A.; Marino, M., An innovative deployable solar panel system for Cubesats. Acta Astronaut., 95 (2014) 210–217.

6. Paolo, G.; Piergentili, F.; Santoni, F., Miniaturized attitude control system for nanosatellites. Acta Astronaut., 81 (2012) 325–334.

7. Li, J.; Post, M.; Wright, T.; Lee, R., Design of Attitude Control Systems for CubeSat-Class Nanosatellite. J. Control Sci. Eng., (2013).

8. Jansen, T.; Reinders, A.; Oomen, G.; Bouwmeester, J., Performance of the first flight experiment with dedicated space CIGS cells onboard the Delfi-C3 nanosatellite. 35th IEEE Photovolt. Spec. Conf., 31 (2010) 1128–1133.

9. Reif, A.W.; Hoang, V.; Kalman, A.E., Recent Advances in the Construction of Solar Arrays for CubeSats, in: CubeSat Summer Dev. Work. 24th Annu. AIAA/USU Conf. Small Satell., 2010: pp. 1–18.

10. Ve, I.; Hrouda, J.; Hofman, J., Spectrolab Triangular Solar Cell Evaluation for Usage in PilsenCUBE Picosatellite, in: Proc. Int. Conf. Appl. Electron., 2010: pp. 1–14.

11. Mahdi, M.C.; Hassan, A.F.; Jaafer, J.S., New deployable solar panel array for 1U nanosatellites. ARPN J. Eng. Appl. Sci., 9 (2014) 2322–2326.

12. McGuire, T.; Hirsch, M.; Parsons, M.; Leake, S.; Straub, J., A CubeSat deployable solar panel system. Proceeding SPIE, 9865 (2016) 1–8.

13. Miguel, J.; Plaza, E.; Antonio, J.; Vilán, V.; Agelet, F.A.; Barandiarán, J.; Estévez, M.L.; Fernández, C.M.; Ares, F.S., Xatcobeo : Small Mechanisms for CubeSat Satellites – Antenna and Solar Array Deployment. Proc. 40th Aerosp. Mech. Symp., (2010) 415–429.

14. Senatore, P.; Klesh, A.; Zurbuchen, T.H.; Mckague, D.; Cutler, J., Concept , Design , and Prototyping of XSAS : A High Power Extendable Solar Array for CubeSat Applications. Proc. 40th Aerosp. Mech. Symp., (2010) 431–444.

15. Passaretti, M.; Hayes, R., Development of a Solar Array Drive Assembly for

CubeSat. Proc. 40th Aerosp. Mech. Symp., (2010) 445–453.

16. MMA Design LLC, Power boost gives mission planners more flexibility to use smaller, lower-cost satellites. (2017). https://www.sbir.gov/sites/default/files/MMADesign_AF093-088.pdf (accessed September 20, 2019).

17. Tethers Unlimited, Sunmill Array - Deployable, steerable solar array for CubeSats. (2012). http://www.tethers.com/SpecSheets/Brochure_SunMillArray.pdf (accessed September 20, 2019).

18. Mcgill, E.; Mcgill, E., Development of a Self-Orienting CubeSat Solar Array, University of Dayton, 2018. https://ecommons.udayton.edu/cgi/viewcontent.cgi?article=1172&context=uhp_theses.

19. Rawashdeh, S.; Jones, D.; Erb, D.; Karam, A.; Lumpp, J.E., Aerodynamic attitude stabilization for ram- facing CubeSat. Adv. Astronaut. Sci., 133 (2009) 1–13.

20. Armstrong, J.; Casey, C.; Creamer, G.; Dutchover, G., Pointing control for low altitude triple CubeSat space darts, in: 23rd Annu. AIAA/USU Conf. Small Satell., 2009.

21. Peters, E.D., Dynamic instabilities imparted by CubeSat deployable solar panels. Master Thesis, Massachusetts Inst. Technol., (2014). https://dspace.mit.edu/handle/1721.1/93800.

22. Bettiol, L., Dynamic analysis of thin-film solar panels on small satellites, 2014. http://tesi.cab.unipd.it/45566/1/tesi_Laura_Bettiol.pdf.

23. Ross, B.; Woo, N.; Smith, Z.; George, S., Simulating CubeSats structure deployment. AIAA SciTech Forum, (2018) 1–17.

24. Vertat, I.; Vobornik, A., Efficient and reliable solar panels for small CubeSat picosatellites. Int. J. Photoenergy, (2014).

25. Horváth, G.; Czifra, D.; Marosy, G.; Várhegyi, Z., Thermal design and characterization of solar cell arrays aimed to be used in CubeSat missions, in: Proc. 18th Int. Work. Therm. Investig. ICs Syst., 2012.

26. Sanchez-sanjuan, S.; Gonzalez-llorente, J.; Hurtado-velasco, R., Comparison of the Incident Solar Energy and Battery Storage in a 3U CubeSat Satellite for Different Orientation Scenarios. 8 (2016) 91–102.

27. Bandyopadhyay, S.; Foust, R.; Morgan, D.; Hadaegh, F.Y., A Review of Impending Small Satellite Formation. 53rd AIAA Aerosp. Sci. Meet., (2015) 1–17.

28. Williams, T.; Wang, Z., Uses of solar radiation pressure for satellite formation flight. Int. J. Robust Nonlinear Control 2002, 183 (2002) 163–183.

29. Mishne, D.; Edlerman, E., Collision-Avoidance Maneuver of Satellites Using Drag and Solar Radiation Pressure. J. Guid. Control. Dyn., (2016) 1–15.

30. Macdonald, M.; Innes, C.M., Solar sail science mission applications and advancement. Adv. Sp. Res., 48 (2011) 1702–1716.

31. Tsuda, Y.; Mori, O.; Funase, R.; Sawada, H.; Yamamoto, T.; Saiki, T.; Endo, T.; Kawaguchi, J., Flight status of IKAROS deep space solar sail demonstrator. Acta Astronaut., 69 (2011) 833–840.

32. Fu, B.; Sperber, E.; Eke, F., Solar sail technology — A state of the art review. Prog. Aerosp. Sci., (2016) 1–19.

33. Johnson, L.; Whorton, M.; Heaton, A.; Pinson, R.; Laue, G.; Adams, C., NanoSail-D : A solar sail demonstration mission. Acta Astronaut., 68 (2010) 571–575.

34. Steyn, W.H.; Lappas, V., Cubesat solar sail 3-axis stabilization using panel translation and magnetic torquing. Aerosp. Sci. Technol., 15 (2010) 476–485.

35. Lappas, V.; Adeli, N.; Visagie, L.; Fernandez, J.; Theodorou, T.; Steyn, W.; Perren, M., CubeSail : A low cost CubeSat based solar sail demonstration mission. Adv. Sp. Res., 48 (2011) 1890–1901.

36. Ridenoure, R.W.; Munakata, R.; Wong, S.D.; Diaz, A.; Spencer, D.A.; Stetson, D.A.; Betts, B.; Plante, B.A.; Foley, J.D.; Bellardo, J.M., Testing The LightSail Program : Advancing Solar Sailing Technology Using a CubeSat Platform. J. Small Satell., 5 (2016) 531–550.

37. Gohd, C., Solar Sail Success ! LightSail 2 is officially soaring on sunlight. (2019). https://www.space.com/lightsail-2-solar-sail-mission-success.html (accessed September 21, 2019).

38. Thornton, E.A., Thermally induced vibrations, in: Therm. Struct. Aerosp. Appl., American Institute of Aeronautics and Astronautics, Reston, 1996: pp. 343–395.

39. Thornton, E.A.; Kim, Y.A., Thermally-induced bending vibrations of a flexible rolled-up solar-array. J. Spacecr. Rockets, 30 (1993) 438–448.

40. Wei, L.; Zhihai, X.; Lejin, C.; Mingde, X., Thermal flutter analysis of large-scale space structures based on finite element method. Int. J. Numer. Methods Eng., (2007) 887–907.

41. Duan, J.; Xiang, Z.; Xue, M., Thermal - dynamic coupling analysis of large space structures considering geometric nonlinearity. Int. J. Struct. Stab. Dyn., 8 (2008) 569–596.

42. Johnston, J.D.; Thornton, E.A., Thermally induced attitude dynamics of a spacecraft with a flexible appendage. J. Guid. Control Dyn., 21 (1998) 581–587.

43. Johnston, J.D.; Thornton, E.A., Thermally induced dynamics of satellite solar panels. J. Spacecr. Rockets, 37 (2000) 604–613.

44. Iwata, T.; Kazuro, M.; Hiroki, H., Thermally induced dynamics of large solar array paddle - from laboratory experiment to flight data analysis, in: AIAA Guid. Navig. Control Conf., AIAA, Portland, Oregon, 2011.

45. Lee, H.; Yamasaki, M.; Murozono, M., Experimental verification of thermal structural responses of a flexible rolled-up solar array. Trans. Jpn. Soc. Aeronaut. Space Sci., 56 (2013) 197–204.

46. Shin, K.; Kim, C.; Hong, C.; Lee, H., Thermal distortion analysis of orbiting solar array including degradation effects of composite materials. Compos. Part B Eng., 32 (2001) 271–285.

47. Li, J.; Yan, S., Thermally induced vibration of composite solar array with honeycomb panels in low earth orbit. Appl. Therm. Eng., 71 (2014) 419–432.

48. Liu, J.; Pan, K., Rigid-flexible-thermal coupling dynamic formulation for satellite and plate multibody system. Aerosp. Sci. Technol., 52 (2016) 102–114.

49. Azadi, E.; Fazelzadeh, S.A.; Azadi, M., Thermally induced vibrations of smart solar panel in a low-orbit satellite. Adv. Sp. Res., 59 (2017) 1502–1513.

50. Ubbels, W.J.; Bonnema, A.K., Delfi-C3: A student nanosatellite as a test-bed for thin film solar cells and wireless onboard communication, in: Proc. 2nd Int. Conf. Recent Adv. Sp. Technol., IEEE, 2005: pp. 167–172.

51. Mehrparvar, A., CubeSat design specification, revision 13. (2014). http://www.cubesat.org/resources/ (accessed September 1, 2016).

52. Qioptiq, Qioptiq solar cell coverglasses. (2017). http://www.qioptiq.com/download/QST_2015_03_Datasheet_CoverGlass v3[1].pdf (accessed December 28, 2017).

53. Crystan, Crystran Gallium Arsenide (GaAs). (2017). https://www.crystran.co.uk/optical-materials/gallium-arsenide-gaas (accessed December 28, 2017).

54. DielectricCorporation, Dielectric Corporation Glass-Epoxy. (2018). http://www.dielectriccorp.com/downloads/thermosets/glass-epoxy.pdf (accessed December 28, 2017).

55. Beex, L.A.A., Warpage of printed circuit, Eindhoven University of Technology, 2005. www.mate.tue.nl/mate/pdfs/5338.pdf.

56. Azar, K.; Graebner, J., Experimental determination of thermal conductivity of printed wiring boards. Proc. Twelfth IEEE SEMI-THERM Symp., (1996) 169–182.

57. Paggi, M.; Kajari-Schröder, S.; Eitner, U., Thermomechanical deformations in photovoltaic laminates. J. Strain Anal. Eng. Des., 46 (2011) 772–782.

58. Shimada, T.; Toyota, H.; Hirose, K.; Maeda, Y.; Mitsuda, K., On-orbit performance analysis on solar array paddle of X-ray astronomy satellite “Suzaku.” 2014 IEEE 40th Photovolt. Spec. Conf. PVSC 2014, (2014) 2161–2165.

59. Endurosat, 3U single deployable solar array. (2018). https://www.endurosat.com/cubesat-store/all-cubesat-modules/3u-single-deployable-solar-array/ (accessed October 25, 2018).

60. Innovative Solutions in Space, ISIS CubeSat solar panels. (2018). https://www.isispace.nl/product/isis-cubesat-solar-panels/ (accessed October 20, 2018).

61. SpaceQuest, SP-C CubeSat solar panels. (2018). http://www.spacequest.com/shop2/sp-6 (accessed October 21, 2018).

62. Panczak, T.D.; Schmidt, M.J.; Bell, D.P.; Cullimore, B.A., CRTech TD Direct User's Guide Version 5.8, 2016.

63. Cullimore, B.A.; Ring, S.G.; Johnson, D.A., SINDA/FLUINT User's Manual Version 5.8, 2015.

64. Boley, B., Approximate analyses of thermally induced vibrations of beams and plates. J. Appl. Mech., 39 (1972) 212–216.

65. Abaqus, Getting started with Abaqus: Interactive Edition, Version 6., Dassault Systemes Simulia Corp., 2012.

66. Abbas, L.K.; Chen, D.; Rui, X.; Abbas, L.K.; Chen, D.; Rui, X., Numerical calculation of effect of elastic deformation on aerodynamic characteristics of a rocket. Int. J. Aerosp. Eng., 2014 (2014).

67. Sleight, D.; Muheim, D., Parametric studies of square solar sails using finite element analysis. 45th AIAA/ASME/ASCE/AHS/ASC Struct. Struct. Dyn. Mater. Conf., (2004) 1–13.

68. Nelson, M.F.; Wolf, J.A., The Use of Inertia Relief to Estimate Impact Loads. SAE Tech. Pap. 770604, (1977) 2237–2243.

69. X. Meyer, R., Elements of space technology for aerospace engineers, Academic Press, 1999.

70. Rawashdeh, S.A.; Lumpp, J.E., Aerodynamic stability for CubeSats at ISS orbit. J. Small Satell., 2 (2013) 85–104.

71. Paluszek, M.; Bhatta, P.; Griesemer, P.; Mueller, J.; Thomas, S., Spacecraft attitude and orbit control Volume 1: A systems approach, 3rd ed., Princeton satellite systems, 2012.

72. Wertz, J., Spacecraft attitude determination and control, Kluwer Academic Publishers, 1978.

73. Springmann, J.; Cutler, J.; Bahcivan, H., Magnetic Sensor Calibration and Residual Dipole Characterization for Application to Nanosatellites, in: AIAA/AAS Astrodyn. Spec. Conf. Guid. Navig. Control, 2010.

74. Pumpkin Inc, CubeSat kit - in space. (2018). http://www.cubesatkit.com/content/space.html (accessed December 13, 2018).

75. Clyde Space, Clyde Space Products. (2019). https://www.clyde.space/products (accessed January 21, 2019).

76. Sondecker IV, G.; La Tour, P.; Abramowitz, L., SENSE: The USAF SMC/XR NanoSatellite Program for Space Environmental Monitoring Capt, in: 27th Annu. AIAA/USU Conf. Small Satell., 2013.

77. Rodrigo, J.; Alarcon, C.; Kim, S.; Cho, M., Aoba VELOX-IV Attitude and Orbit Control System Design for a LEO Mission Applicable to a Future Lunar Mission, in: 67th Int. Astronaut. Congr., 2016.

78. Jenkins, A., The Sun's position in the sky. Eur. J. Phys., (2013) 633–652.

79. L. Rickman, S.; R. Ortiz Longo, C., Method for the Calculation of Spacecraft Umbra and Penumbra Shadow Terminator Points Method for the Calculation of Spacecraft Umbra and Penumbra Shadow Terminator Points. (1995). https://ntrs.nasa.gov/archive/nasa/casi.ntrs.nasa.gov/19950023025.pdf (accessed January 21, 2019).

80. Srivastava, V.K.; Yadav, S.M.; Kumar, J.; Kushvah, B.S., Earth conical shadow modeling for LEO satellite using reference frame transformation technique : A comparative study with existing earth conical shadow models. Astron. Comput., 9 (2015) 34–39.

81. Ismail, M.N.; Bakry, A.; Selim, H.H.; Shehata, M.H., Eclipse intervals for satellites in circular orbit under the effects of Earth's oblateness and solar radiation pressure. NRIAG J. Astron. Geophys., 4 (2015) 117–122.

82. Princeton Satellite Systems, CubeSat Toolbox. (2018). http://www.psatellite.com/products/sct/cubesat-toolbox/ (accessed December 13, 2018).

83. Sidi, M.J., Spacecraft dynamics and control, Cambridge University Press, London, 1997.

84. Ibrahim, S.A.; Yamaguchi, E., Thermally induced dynamics of deployable solar panels of nanosatellite. Aircr. Eng. Aerosp. Technol., (2019) AEAT-07-2018-0185.

85. JAXA, JEM Small Satellite Orbital Deployer (J-SSOD). (2018). http://iss.jaxa.jp/en/kiboexp/jssod/ (accessed December 21, 2018).

86. Crusan, J.; Galica, C., NASA's CubeSat Launch Initiative : Enabling broad access to space. Acta Astronaut., (2018) 1–10.

Publications

Journal Articles

1. Syahrim Azhan Ibrahim and Eiki Yamaguchi, Thermal distortion on Deployable Solar Panels of CubeSat in Low Earth Orbit, *Volume 165 of the Advances in the Astronautical Sciences Series*, pp. 2107-2117, 4th IAA Conference on Dynamics and Control of Space Systems, DyCoSS'2018.
2. Syahrim Azhan Ibrahim and Eiki Yamaguchi (2019), Thermally induced dynamics of deployable solar panels of nanosatellite, *Aircraft Engineering and Aerospace Technology*, Vol.91 No.7, pp.1039-1050. https://doi.org/10.1108/AEAT-07-2018-0185.
3. Syahrim Azhan Ibrahim and Eiki Yamaguchi, Comparison of solar radiation torque and power generation of deployable solar panels configurations on nanosatellite, *Aerospace 2019, 6(5), 50*. https://doi.org/10.3390/aerospace6050050.

Conferences

1. Syahrim Azhan Ibrahim, Eiki Yamaguchi, Thermal bending analysis on orbiting deployable solar panels of nanosatellite, *4th International Symposium on Applied Engineering and Sciences*, December, 2016.
2. Syahrim Azhan Ibrahim, Eiki Yamaguchi, Thermal distortion on deployable solar panels of CubeSat in Low Earth Orbit, *4th International Academy of Astronautics Conference on Dynamics and Control of Space Systems*, May, 2018.
3. Syahrim Azhan Ibrahim, Eiki Yamaguchi, Study of solar disturbance torque on CubeSat deployable solar panels, *6th International Symposium on Applied Engineering and Sciences*, December, 2018.